Draft version November 21, 2022
Typeset using LaTeX default style in AASTeX62

arXiv:2211.10063v1 [astro-ph.GA] 18 Nov 2022

WISE Green Objects (WGOs): the massive star candidates in the whole Galactic Plane ($| b |< 2°$)

Chang Zhang,[1,2] Guo-Yin Zhang,[1] Jin-Zeng Li,[1] and Jing-Hua Yuan[1]

[1] *National Astronomical Observatories, Chinese Academy of Sciences, A20 Datun Road, Chaoyang District, Beijing 100101, PR China; zhangc@nao.cas.cn, zgyin@nao.cas.cn, ljz@nao.cas.cn*

[2] *University of Chinese Academy of Sciences, Beijing 100049, PR China*

(Received June 28, 2022; Revised October 31, 2022; Accepted November 12, 2022)

Submitted to ApJS

ABSTRACT

Massive young stellar objects (MYSOs) play a crucial role in star formation. Given that MYSOs were previously identified based on the extended structure and the observational data for them is limited, screening the Wide-field Infrared Survey Explorer (WISE) objects showing green features (for the common coding of the 4.6 μm band as green channel in three-color composite WISE images) will yield more MYSO candidates. Using WISE images in the whole Galactic Plane ($0° < l < 360°$ and $| b |< 2°$), we identified sources with strong emissions at 4.6 μm band, then according to morphological features divided them into three groups. We present a catalog of 2135 WISE Green Objects (WGOs). 264 WGOs have an extended structure. 1366 WGOs show compact green feature but without extended structure. 505 WGOs have neither extended structure nor green feature, but the intensity at 4.6 μm is numerically at least 4.5 times that of 3.4 μm. According to the analysis of the coordinates of WGOs, we find WGOs are mainly distributed in $| l |< 60°$, coincident with the position of the giant molecular clouds in $| l |> 60°$. Matching results with various masers show that those three groups of WGOs are at different evolutionary stages. After cross-matching WGOs with published YSO survey catalogs, we infer that ∼50% of WGOs are samples of newly discovered YSOs. In addition, 1260 WGOs are associated with Hi-GAL sources, according to physical parameters estimated by spectral energy distribution fitting, of which 231 are classified as robust MYSOs and 172 as candidate MYSOs.

Keywords: ISM: WISE Green Objects — ISM: Outflow – stars: formation — stars: massive—stars: protostars

1. INTRODUCTION

As the main contributor to emission and chemical enrichment of the universe, the formation of stars has invariably been an important research topic in astronomy. The scenario of low-mass star formation has been well established (Shu et al. 1987). Statistics suggest that massive star formation is unlikely to be found nearby, with most being > 2 kpc away. Influenced by the factors such as star-forming regions are rare, deeply embedded, the timescales are extremely short, and the natal environments are inevitably destroyed by violent feedback, the formation process of the massive star ($\gtrsim 8\ M_{\odot}$) is still a mystery (Zinnecker & Yorke 2007). The result of these observational obstacles is that there are few accurate or well-selected samples of objects in the early stages of evolution. A large, unbiased sample of massive young stellar objects (MYSOs), especially those in infancy, could help understand the processes involved in the formation and earliest stages of massive star formation (Urquhart et al. 2014, 2022).

The "monolithic collapse" model (McKee & Tan 2002, 2003) and the "competitive accretion" model (Bonnell et al. 1997; Bonnell & Greaves 2004) are two popular models of massive star formation. The "monolithic collapse" model is an extended version of low-mass star formation, in which gas is accreted onto the protostar through an accretion disk at a significantly higher rate of accretion compared to its low-mass star formation. The final stellar mass comes from

Corresponding author: Chang Zhang, Guo-Yin Zhang, Jin-Zeng Li

the initial core mass in this model. The "competitive accretion" model is that massive stars always form in clusters and rely on the competitive accumulation of cluster members from a common envelope. The final stellar mass depends on the result of the competition. Regardless of the mass, there is evidence of the same nature of low- and high-mass star formation. For example, the latest findings of accretion bursts in MYSO (e.g., Caratti o Garatti et al. 2017; Stecklum et al. 2017, 2021) reveal that both low- and high-mass protostars form through disk accretion, accompanied by episodic accretion bursts, possibly caused by disk fragmentation. The typical the accretion rate during the low-mass star formation is $\sim 5 \times 10^{-6}$ $M_{\odot}$ yr^{-1} (Hosokawa et al. 2010). In estimating this value, a typical dust temperature of 10 K in the cold core is adopted (Zhang et al. 2022). This value during massive star formation is expected to be $\gtrsim 10^{-4}$ $M_{\odot}$ yr^{-1} (Hosokawa et al. 2010). Such high accretion rates support the ability of lower-mass progenitors have the ability to accrete enough material from their gas-rich circumstellar disks to grow into massive stars (e.g., Motte et al. 2018; Chen et al. 2021).

The MYSO samples were determined mainly by observational data provided by *IRAS* (Molinari et al. 1996) and the *Midcourse Space Experiment* (*MSX*) (Hoare et al. 2005), while the *Spitzer* surveys of the Galactic Plane using the InfraRed Array Camera (IRAC, 3.6, 4.5, 5.8 and 8.0 μm; Fazio et al. 2004) that came later replaced the former with sub-2″ resolution and higher sensitivity. The *Spitzer* Galactic Legacy Infrared Mid-Plane Survey Extraordinaire (GLIMPSE, Churchwell & GLIMPSE Team 2001) I / II has revealed several "Extended Green Objects" (EGOs) which display extended emission in the 4.5 μm band coded as the green channel in the trichromatic image. The extended green emission is thought to be caused by MYSO outflows (Cyganowski et al. 2008; Chen et al. 2013). When the material is continually accreted from the disk to the protostar, it will release excess angular momentum and produce collimated jets or outflows (e.g., Shu et al. 1987; Hosokawa et al. 2010; Motte et al. 2018; Chen et al. 2021). The *Spitzer* 4.5 μm band covers excitation radiation of H_2 ($v = 0 - 0$, S (9, 10, 11)) and CO ($v = 1 - 0$) that forms in the regions of interaction between outflows and interstellar medium (Smith & Rosen 2005; Reach et al. 2006; Davis et al. 2007). The sources with extended 4.5 μm emission have a high percentage of shock-triggered masers (e.g., H_2O and CH_3OH Class I, Cyganowski et al. 2009, 2013; Chen et al. 2011; Towner et al. 2017). As the signposts of MYSOs, class II methanol masers have a high detection rate in MYSOs (Jones et al. 2020; Stecklum et al. 2021). The above evidences show that the EGOs are excellent MYSO candidates with active outflows.

The *Spitzer* observation range is limited to the inner Galactic Plane ($| l | < 65°$, Churchwell et al. 2009). The observation area of Wide-field Infrared Survey Explorer (WISE) covers the entire Galactic Plane (Wright et al. 2010). The exposure time of *Spitzer* GLIMPSE is 4 seconds per frame, and 5σ sensitivity is $\sim$ 0.2 mJy at 4.5 μm band (Benjamin et al. 2003). The exposure time of WISE is 11 seconds per frame, and 5σ sensitivity is $\sim$ 0.11 mJy at 4.6 μm band (Wright et al. 2010). Although WISE has an angular resolution about 3 times smaller than that of *Spitzer*, but thanks to the long exposure time of WISE, the sensitivity of WISE is 2 times higher than that of *Spitzer*. In addition, the WISE data we adopted is $\sim$1440 deg^2, which is five times of *Spitzer* GLIMPSE ($\sim$274 deg^2). Considering sample size = (solid angle)*N(>S) where N(>S) is the surface number density of sources brighter than a flux limit S, and N(>S) $\sim$ 1/S, WISE is expected to find ten times as many sources as *Spitzer*.

Cyganowski et al. (2008) and Chen et al. (2013) identified MYSOs by checking whether the infrared sources have extended structures. In this work, WISE W1, W2, and W3 bands are encoded as blue, green, and red, respectivley, in the three-color composite images. We call sources that appear green in color or sources whose W2 is significantly larger than W1 in value as WGOs. Dense cores are localized density enhancements of the cloud material that have been recognized for sites of low- and high mass star formation for more than 30 years (Bergin & Tafalla 2007). WGOs, which do not show 4.6 μm extended emission, are still deeply embedded in the cores and may be at an early evolutionary stage of MYSOs. As long as there is enough gas on the envelope or disk, they have the potential to grow into MYSOs with extended structures (Jijina & Adams 1996; Yorke & Sonnhalter 2002). The ultra-low temperature cooled cameras carried by *Herschel* can detect far-infrared dust radiation from the dense cores (Pilbratt et al. 2010). Based on the size and mass of the core, it can be inferred whether the core can give birth to massive stars (e.g., Krumholz & McKee 2008; Kauffmann & Pillai 2010; Zhang et al. 2018). The emission of YSOs in different bands will change with the evolution process and this change is reflected in the shape of the spectrum energy distribution (SED) fitting (e.g., Shu et al. 1987; Lada 1987; Andre et al. 1993; Greene et al. 1994). By fitting the SED of YSOs with the corresponding theoretical model (Robitaille 2017), we can obtain various property parameters of YSOs, such as mass, temperature, and radius. By combining these parameters, the accretion rate of YSOs can be estimated, which can predict whether YSOs can form massive stars (e.g., Moser et al. 2020; Jones et al. 2019; Stecklum et al. 2021).

Table 1. Objects in SIMBAD used to rule out possible evolved targets.

Object Type in SIMBAD	Object Type in SIMBAD
Star	Nova
OH/IR star	Post-AGB Star
Carbon Star	Nova-like Star
Variable Star	Mira candidate
Wolf-Rayet Star	Planetary Nebula
Emission-line Star	AGB Star candidate
Possible Carbon Star	Post-AGB Star Candidate
Long-period variable star	Possible Planetary Nebula
Variable Star of RR Lyr type	Variable Star of Mira Cet type
Asymptotic Giant Branch (AGB) Star	

The outline of the paper is as follows. In Sect. 2, we describe archived data used for this article. Data analysis and results are presented in Sect. 3. Sect. 4 discusses star formation scenario of WGOs and reliability of WGOs as MYSOs. We summarize our conclusions in Sect. 5.

2. ARCHIVE DATA

2.1. *WISE data*

WISE, equipped with a 40 cm diameter infrared telescope, performed an all-sky astronomical survey in Earth orbit over ten months in four infrared bands, W1, W2, W3, and W4, centered at 3.4, 4.6, 12, and 22 μm wavelength (Wright et al. 2010). The angular resolutions are 6.1″, 6.4″, 6.5″, and 12.0″ respectively for wavelengths of 3.4, 4.6, 12, and 22 μm, and in unconfused regions on the ecliptic point source sensitivities at 5σ are better than 0.08, 0.11, 1, and 6 mJy. The data were released on 14 March 2012 and can be retrieved from the Infrared Science Archive[1]. We selected all the data in the range of the Galactic Plane ($\mid b \mid < 2^\circ$) covering $\sim$ 1440 deg^2, including a total of $\sim$600 small images with the size of 1.56°$\times$ 1.56°.

2.2. *Hi-GAL data*

Herschel infrared Galactic Plane Survey (Hi-GAL) was performed in five infrared continuum bands between 70 and 500 μm to map the dust distribution in $\mid b \mid < 1.5^\circ$ (Molinari et al. 2010), that provide a census of dense and cold condensations that some sources may have harbored YSOs. Mège et al. (2021) resolved distances for $\sim$80% compact sources by substituting radial velocity into the rotation of the Galaxy and assisted with H I self-absorption method or distance–extinction data to solve distance ambiguity. Based on the fitting of a modified black-body (grey-body) function to *Herschel* $\lambda \geqslant 160$ μm portion and the distances given by Mège et al. (2021), Elia et al. (2021) derived source physical properties, including the mass M, the temperature T, and bolometric luminosity L and so on. The source size is measured from 250 μm wavelength image.

3. DATA ANALYSIS AND RESULTS

3.1. *Identification and Classification of WGOs*

We introduce detailed process of screening WGOs in this section. We first divide the W2 image by the W1 image pixel by pixel, pixels with an intensity ratio greater than 1.7 are retained, and those less than 1.7 are discarded, after that, sources with a size $\gtrsim$ one beam (6″ $\times$ 6″) were extracted as "Raw Sample". Then, we matched the "Raw Sample" and ALLWISE source catalog (Wright et al. 2019) within 6″ and obtained 17311 "WISE Associations". YSOs with thick accretion disks usually radiate significantly in the 12 or 22 μm and can be detected even at substantial distances (Wright et al. 2010). So we further selected the samples with emission in the 12 or 22 μm to ensure that they are YSOs in an early accretion stage. In addition, based on our investigation, the ratio of W2 and W1 of most (over 80%)

[1] https://irsa.ipac.caltech.edu/Missions/wise.html

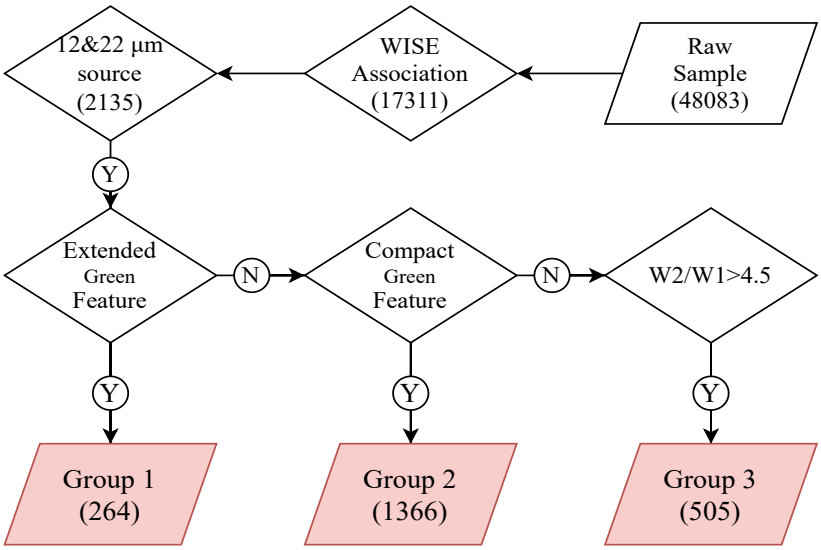


Figure 1. Flowchart describing the identification procedure of WGOs.

identified EGOs in WISE is greater than 4.5. So according to this feature, if the ratio of the intensity of the 4.6 μm band to the intensity of the 3.4 μm band is more significant than 4.5, such a source we also temporarily consider as WGOs. WGOs cannot be directly identified by the ratio of 4.6 μm to 3.4 μm band alone, and this feature also appears in the late stages of some stellar evolution, such as asymptotic giant branch (AGB) star (Busso et al. 1999; Herwig 2005), which makes us confuse them with WGOs. Therefore, we rule out possible targets in Table 1 from WGOs candidates with non-green features by cross-identifications with the SIMBAD database in 6″ (WISE approximate resolutions at 3.4, 4.6, and 12 μm), which contains valuable object type information of our targets (Wenger et al. 2000). Fig. 1 is a flow chart for identifying WGOs and the final number of the WGOs is 2135.

To effectively identify the extended or compact green objects, we displayed WISE 3-color image into about 2.43 deg^2 (1.56°× 1.56°) mosaics, in which 3.4 μm (W1) band for blue channel, 4.6 μm (W2) band for green channel, 8.0 μm (W3) band for red channel. In addition, images of W2/W1 in the same format as the 3-color images were also made to search for WGOs that were not green. Each image was independently visually searched twice by the three authors of this paper, and only WGOs approved by all three were added to the catalog. All WGOs are divided into three sub-catalogs according to morphological features and the intensity ratio of W2 and W1 (Fig. 1). Extended green structure is an obvious external feature of MYSO. WGOs with extended green structures are classified as Group 1, with detailed selection criteria being that the ratio of the major axis to the minor axis of the source is $\gtrsim$ 1.2. WGOs with green compact morphology but without extended structure are classified into Group 2. Group 3 has no apparent green color feature, but its intensity ratio of W2 and W1 is more significant than 4.5. Fig. 2 shows an example of the WGOs in Groups 1, 2, and 3. Since groups 2 and 3 do not yet have extended structures formed by outflow activity, they may be younger than traditional EGOs and may be MYSO candidates at an early stage. The number of groups 1, 2, and 3 are 264, 1366, and 505, accounting for 12%, 64%, and 24% of the total.

3.2. *Galactic distribution of the WGOs*

2135 WGOs are shown in Fig. 3a. 1578 WGOs are in $|\ l\ |< 60°$, which make up 74% of the total sample. WGOs in $|\ l\ |< 60°$ are not symmetrically distributed. 709 WGOs locate in the range of [0°, 60°] with a peak at ∼15°. 869 WGOs locate in [-60°, 0°] with a peak at ∼25°. The number in [-60°, 0°] is 20% more than that in [0°, 60°]. 556 WGOs are in $|\ l\ |> 60°$. WGOs mainly distributed in $75° < l < 85°$, $105° < l < 115°$, $130° < l < 135°$, $-105° < l < -95°$ and $-155° < l < -135°$ regions, which are coincident with the locations of the Cygnus, Cepheus, Cassiopeia, Vela and Monoceros giant molecular clouds respectively.

As the parent structure of the YSO, the size and mass of the Hi-GAL compact source determine the potential to form the massive star. We cross-matched WGOs and Hi-GAL compact source catalog, and found 1260 WGOs have Hi-GAL source counterparts. Among them, 1151 sources have complete information from Elia et al. (2021), such as heliocentric distance, luminosity, mass, and temperature. We adopt the distance of the Hi-GAL sources as the distance

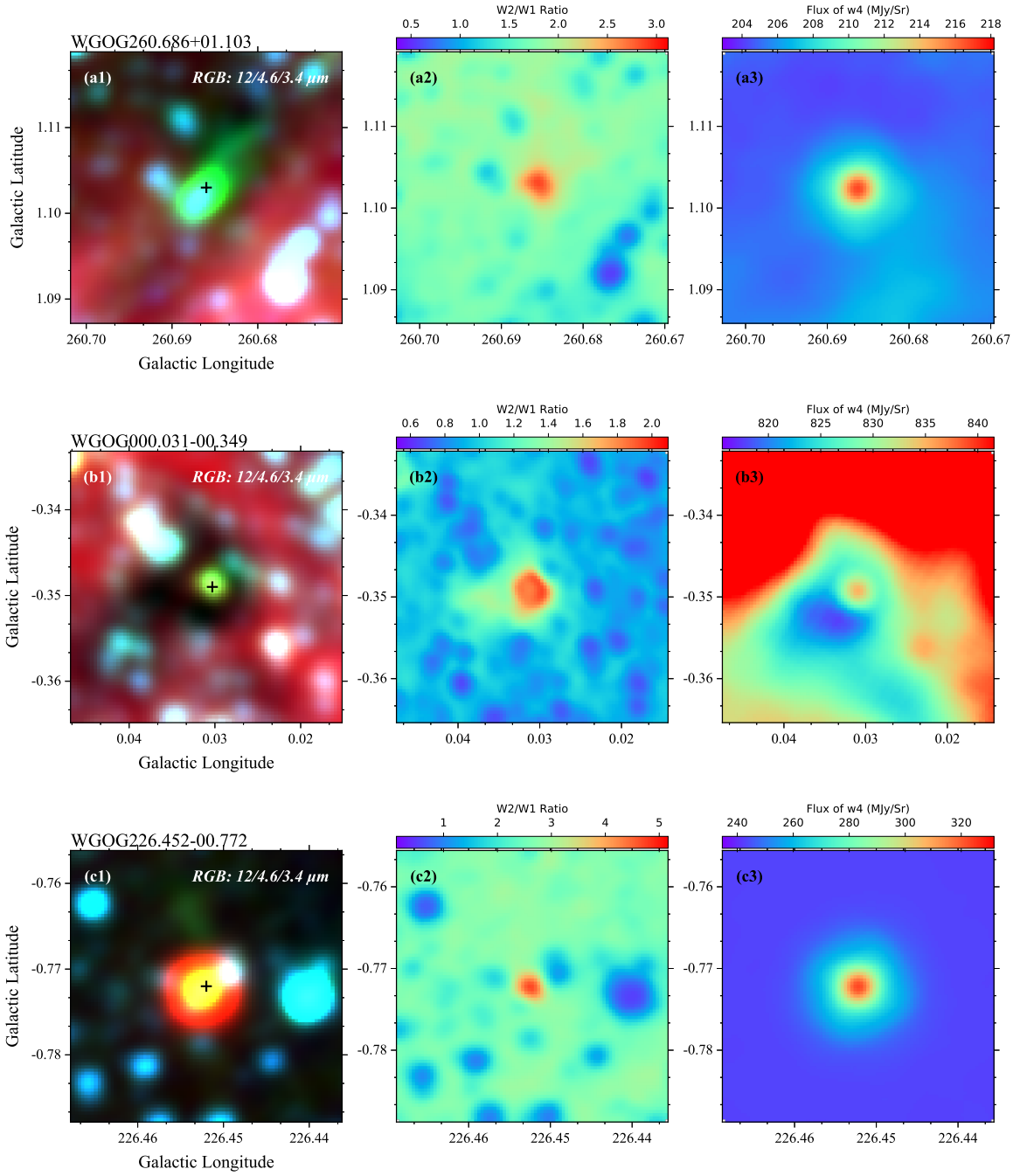


Figure 2. Morphology of the exemplary WGOs. Panels a, b, c represent groups 1, 2 and 3. Panels a1, b1, c1 are trichromatic maps of emission at 3.4, 4.6, 12 microns, rendered in blue, green, and red. Panels a2, b2, c2 are W2/W1 ratio maps. Panels a3, b3, c3 show 22 μm images. Black cross marks the center of each WGO.

of the corresponding WGOs. Fig. 4 gives an overview of the distribution of those 1151 WGOs in the Milky Way viewed from the north Galactic pole. If we only infer the distribution of WGOs from Fig. 3, an erroneous conclusion will be obtained, that WGOs are concentrated in the Galactic Center, because the projection effect is not considered. But in Fig. 4 we can see that most of the WGOs are distributed along the spiral arm. Many WGOs in the line-of-sight direction are just projected to the CMZ, but the actual distance is not that far.

The red dashed line in Fig. 3b shows the distribution of WGOs on the Galactic latitude ($\mid b \mid < 2^\circ$), which can be well fitted with a Gaussian curve, with FWHM of 1° and a peak of ∼150. In the FWHM range ($\pm 1^\circ$) of this Gaussian

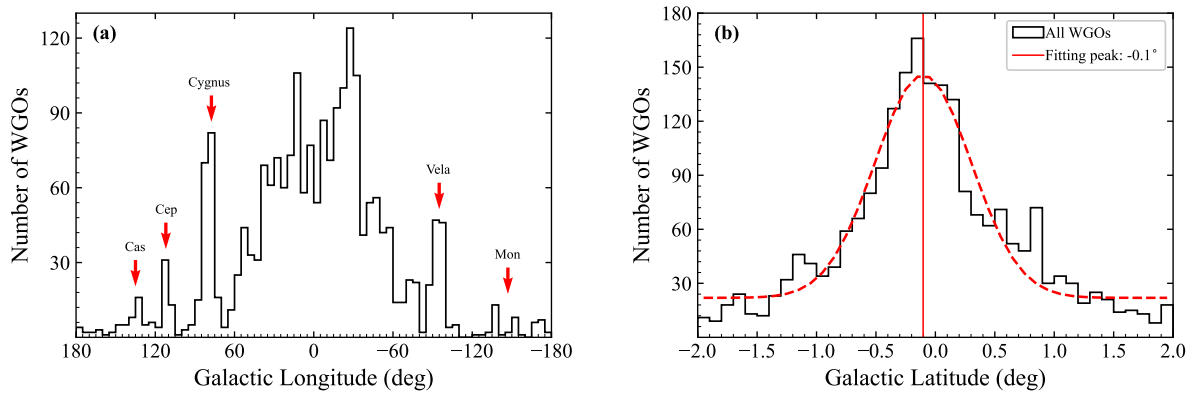


Figure 3. Panel (a) is the number distribution of WGOs as a function of Galactic longitude in 5° bins. The locations of giant molecular clouds are indicated by red arrows. The panel (b) is number distribution of WGOs as a function of Galactic latitude in 0.1° bins and fitted with a Gaussian curve. The red vertical line denotes the peak position of the Gaussian curve.

curve, the number of WGOs accounts for 80% of the total sample. The center position of this Gaussian curve is not at the center of the galactic coordinates but shifted to the left by 0.1° (see red vertical line in Fig. 3b). This small offset also exists in the distribution of the core or clump structures such as the ATLASGAL survey (Schuller et al. 2009) and the Hi-GAL survey, with negative peak of latitude (b = -0.05° and -0.09° respectively). This may be since our solar system is slightly above the Galactic Plane, and the viewing line of sight causes this offset (Schuller et al. 2009), but Hinz et al. (2009) argues that there are more molecular clouds in positive longitude, obscuring the dense source that results in this offset.

3.3. *Cross-match with previous catalogs*

Using *Spitzer* survery data, Cyganowski et al. (2008) cataloged $\sim$ 300 EGOs and Chen et al. (2013) cataloged 98 EGOs. There are 1401 WGOs in the GLIMPSE I and II survey region (see red and blue regions in Fig. 5). Identification of EGO relies on visual inspection of objects in *Spitzer* 3-color images for the presence of green and extended structures. The identification methods of WGOs are similar to that of EGOs, both are visual inspection, but our adopted sample also include the compact green sources and the sources with excess emission W2/W1$\gtrsim$4.5. We cross-matched our WGOs to *Spitzer* EGOs within 6″ which is equivalent to the resolution of WISE 3.4 and 4.6 μm bands, and found 70, 97 and 41 WGOs in each group are previously discovered EGOs. About half of EGOs do not have a corresponding WGO. After viewing blow-up images for each band of WISE of those unmatched EGOs, we found that the main reason why these EGOs were not picked from the WISE data was the lack of flux in the W3 or W4 bands, which accounted for more than 76% of the EGOs, and the remaining EGOs whose W2/W1 ratio failed to exceed our threshold of 1.7. There is no case where the source blends with adjacent targets due to the low resolution of the WISE and is not recognized.

Due to the constraint of the (approximately $\mid b \mid < 1.5°$) survey range of Hi-GAL (Molinari et al. 2010), 363 WGOs are distributed outside this range, and about 71% (1260/1772) of WGOs have Hi-GAL counterparts within this range. By observing the positions of the remaining nearly 30% WGOs in survey range (see grey points in Fig. 5), we found that some of them located at the edge of the observation field and therefore cannot be effectively identified as sources. However, due to lack of dust emission, the possibility of a few objects in WGOs unrelated to star formation cannot be ruled out. This needs to be further confirmed by follow-up observations. About 36% of the Hi-GAL sources are less than 0.1 pc in size which is the core scale, and the sizes of the remaining 64% are between 0.1 and 1 pc at the clump scale. The median values of the luminosity, mass, and distance are 771 $L_{\odot}$, 320.6 $M_{\odot}$, and 3.7 kpc, respectively. We also cross-matched ATLASGAL YSOs catalog (Urquhart et al. 2022) in inner Galactic Plane ($\mid l \mid < 60°$) without $\mid l \mid < 3°$, and we found that 1176 WGOs cannot match ATLASGAL YSOs.

Kuhn et al. (2021) presented a catalog of $\sim 1.2 \times 10^5$ YSOs based on the *Spitzer*/*IRAS* survey (the inner galactic plane, approximately -105°$< l <$ 110°, $\mid b \mid < 2°$). 1992 WGOs locate at this survey coverage area, and 1095 WGOs match YSOs within 6″. The match rate is 54.9%. Marton et al. (2016) identified over 13300 YSOs using 2MASS and

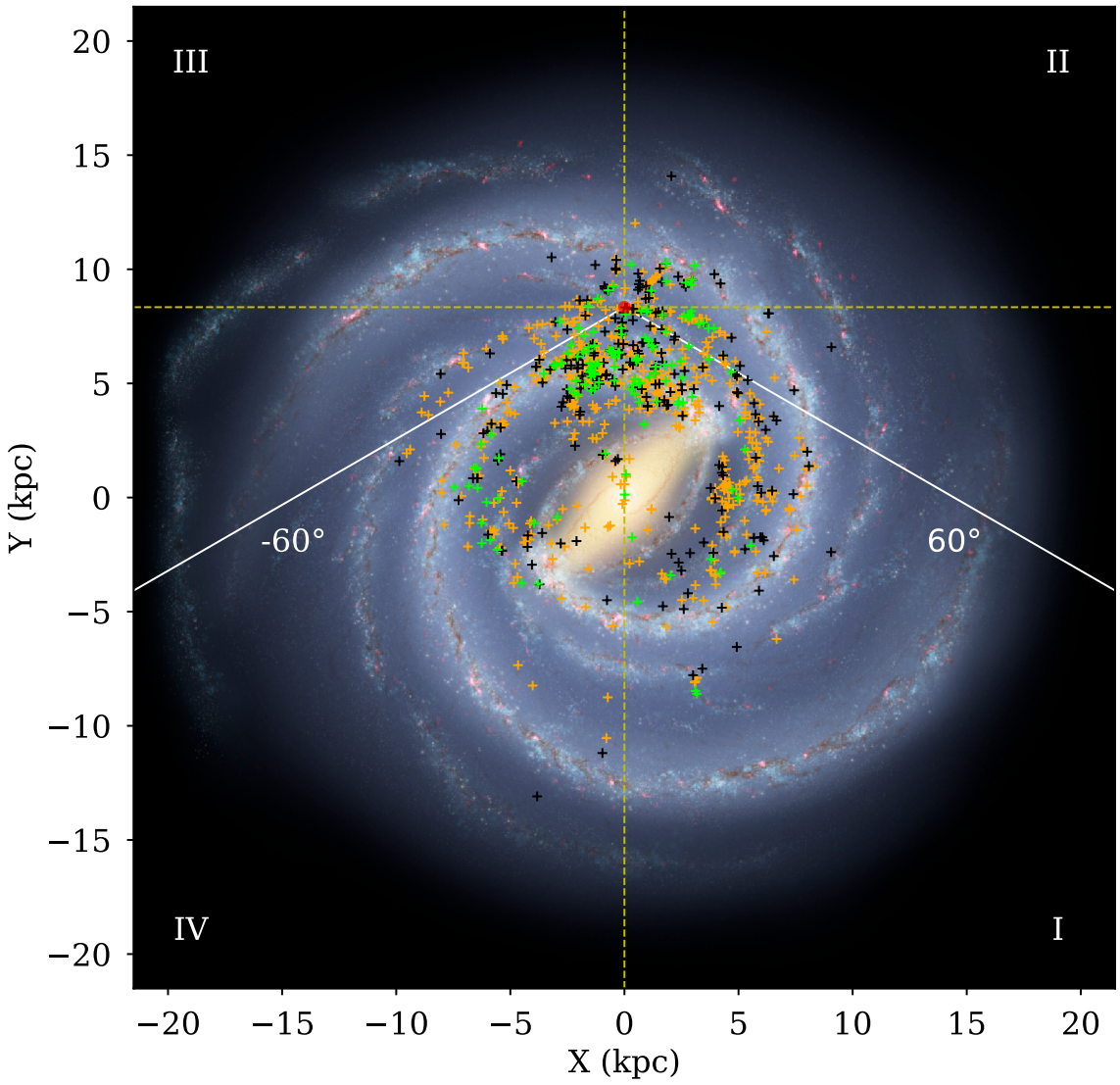


Figure 4. The distribution of WGOs in the Galactocentric system. The axes are Galactocentric distances. We mark the WGOs of three different groups with green, yellow and black crosses, respectively. The background image is a sketch of the Galaxy produced by Robert Hurt (artist's concept, R. Hurt: NASA/JPL- Caltech/SSC). The position of the Sun is shown by the red circle above the Galactic midplane. The two solid white lines enclose the inner Galactic Plane ($|\, l \,| < 60°$).

WISE photometric data combined with support vector machine in all sky. Our WGOs show a low match ratio with this catalog, with only 68 WGOs can match. Meanwhile, the Red *MSX* Source survey (RMS) (Lumsden et al. 2013) provided a catalog with nearly 2800 YSOs, which included 115 MYSOs. 1859 WGOs locate in the range of RMS catalog ($10° < l < 350°$), and we found that 1653 WGOs are newly identified.

3.4. *Cross-match with masers of the star formation indicators*

In the early stage of star formation, MYSOs are deeply embedded within dense molecular cores, with a short accretion period, and remain in the core for a long time even after entering the main sequence phase. Fortunately, large-scale or unique molecular emissions triggered by massive star formation, such as masers, can help identify them (Beuther et al. 2007). We cross-matched WGOs with five masers (CH_3OH Class I/II, H_2O, SiO and OH) related to star formation, using online tool, *MaserDB*[2], provided by Ladeyschikov et al. (2019). Since different distances of WGOs will have a

[2] https://maserdb.net/

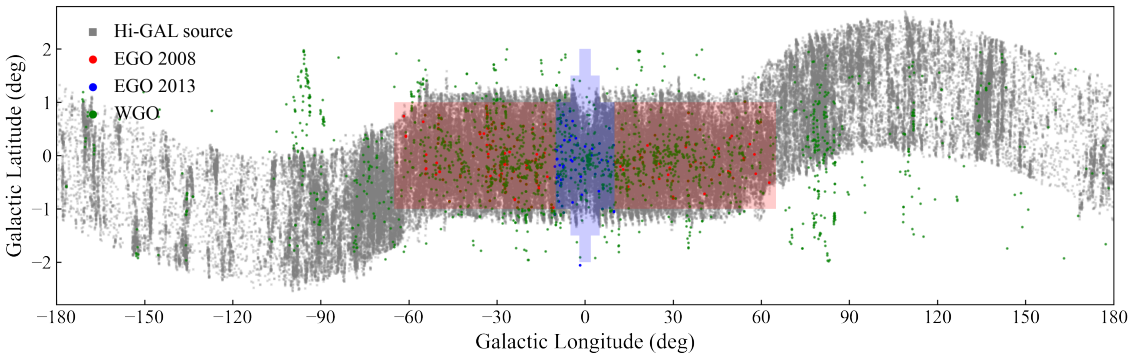


Figure 5. Distribution of WGOs, EGOs and Hi-GAL sources in the galactic plane. Green circles represent WGOs; red and blue circles represent EGOs identified by Cyganowski et al. (2008) and Chen et al. (2013) respectively. The grey points show the Hi-GAL compact sources (Elia et al. 2021). The coverage of GLIMPSE I and II surveys are shaded in red and blue, respectively.

considerable impact on the actual matching radius, and the information on them is incomplete, so we use a uniform matching angular radius that is WISE resolution of 6″, which is corresponding to ∼ 0.15 pc at WGOs mean distance of 5.17 kpc and close to a typical core size (0.1 pc, Zhang et al. 2022). Masers detected by single-dish and interferometric observations have been selected separately. We separately counted the association rate of the WGOs in each group with five kinds of masers and the association rate of WGOs with the cumulative number of masers, which are shown in Fig. 6a and b, respectively. *MaserDB* distinguishes the interferometric positions of methanol Class I/II, H_2O masers from their single-dish positions, but no interferometric positions for OH and SiO masers are provided. Each bar in Fig. 6 shows the association rate of all maser data, including interferometric and single-dish data, and the slash covered portion of each bar shows associated rate of only interferometric maser data. In Fig. 6a, the shape of bars in every kinds of maser, except SiO, are similar, whether it is all maser data or only interferometric data. The most ubiquitous type of masers is water, as it is associated with different astronomical objects (Furuya et al. 2003; Szymczak et al. 2005), at different stages of evolution (e.g., protostellar jets, Hollenbach et al. 2013; large-scale shocks, Mac Low et al. 1994; disks, Gallimore et al. 2003). It is also consistent with the statistical results shown in Fig. 6a. While methanol masers are less ubiquitous. The sub-panel in Fig. 6b more intuitively shows the change of association rate between each group of WGOs and cumulative number of masers. Statistics based on Fig. 6 shows that maserassociation rates in Group 1 are at least 3 and 2 times greater than Groups 2 and 3, and Group 3 is slightly higher than Group 2.

3.5. *Derived physical parameters of the WGOs from the SED models*

We constructed SEDs with WISE four and *Herschel* five wavelengths ranging from 3.4 to 500 μm for 1151 WGOs with Hi-GAL source counterparts. Robitaille (2017) provided 18 kind of model sets for each contain 10,000 models for fitting YSOs in different evolution stage. Based on the prior knowledge of WGOs, there are maybe embedded protostars with an accretion disk or outflow. The model sets we selected are s-smi, sp-smi, sp-hmi, s-p-smi, s-p-hmi, s-pbsmi, s-pbhmi, s-u-smi, s-u-hmi, s-ubsmi, s-ubhmi, spu-smi, and spu-hmi. All 13 model sets contain one or more features, such as envelope or accretion disk or outflow. Fitting the SED of each WGO to the 13 different model sets return χ^2 for each model set. We used $\chi^2 - \chi^2_{\rm best} < 3N_{\rm data}$ as a criterion to select good fits from all model sets. Robitaille (2017) suggested using a Bayesian approach to compare how well among different model sets explain a set of data. $P(D \mid M) \propto N_{\rm good}/N$, where $N_{\rm good}$ is the number of good models from a given model set, and N is the total number of models in that set, is used to indicate the reliability of the model set to the data. In this way, for each WGO, we only need to compare 13 different values of $P(D \mid M)$, and the highest value of $P(D \mid M)$ represents the most suitable model set. We show an example of SED fitting in Fig. 7. Based on the fitting results of the best model set for each WGO, we calculated the mean stellar radius $R_\star$ and surface temperature $T_{\rm eff}$, weighted by $1/\chi^2$. The uncertainties of $R_\star$ and $T_{\rm eff}$ are from weighted standard deviation (e.g., Towner et al. 2019; Chen et al. 2021).

The YSO total luminosity is composed of photospheric luminosity ($L_\star$) and accretion luminosity ($L_{\rm acc}$) (e.g., Chen et al. 2021; Hunter et al. 2021; Olivier et al. 2021)

$$L_{\rm tot} = L_\star + L_{\rm acc} \quad . \tag{1}$$

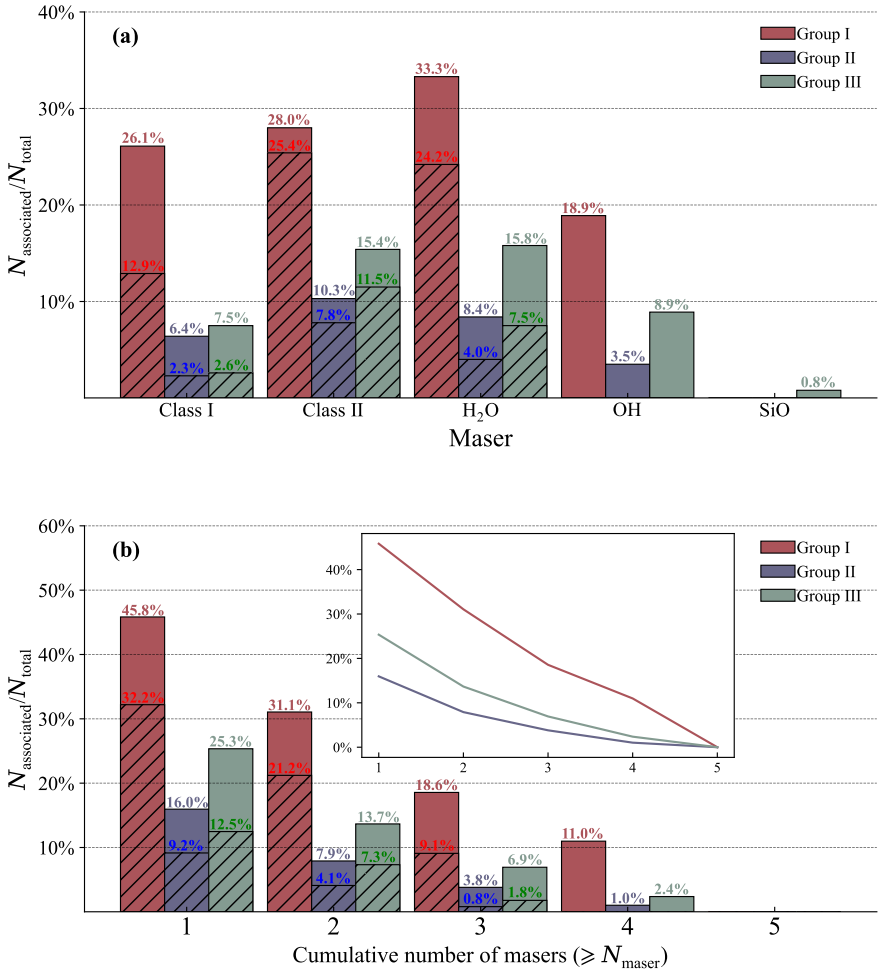


Figure 6. The association rate of the WGOs in each group with five kinds of masers (methanol Class I/II, H_2O, OH, and SiO) (upper panel). $N_{associated}$ is the number of the WGOs associated with the maser. N_{total} is the total number of the WGOs in each group. The red, blue and green bars represent Group 1, 2 and 3 respectively. The lower panel is the association rate of WGOs with the cumulative number of masers ($\geqslant N_{maser}$). $N_{associated}$ in this panel is number of WGOs associated with at least N_{maser} masers. The sub-panel in panel (b) shows the change of association rate between each group of WGOs and cumulative number of masers.

Here we assume all YSOs are absolute blackbody and spherical. According to the Stefan-Boltzmann law, the stellar luminosity $L_\star$ can be derived.

The median values of $L_\star$ in each group of WGOs are 16.6 $L_\odot$, 5.4 $L_\odot$ and 7.4 $L_\odot$ respectively. The median value of $L_\star$ in Group 1 is much larger, perhaps indicating that WGOs in Group 1 are more mature than the other two groups. The accretion rate $\dot{M}_{acc}$ can be estimated from accretion luminosity (Zhang & Tan 2011)

$$L_{acc} = \frac{GM_\star \dot{M}_{acc}}{R_\star} \quad , \tag{2}$$

where G and $M_\star$ are the gravitational constant and mass of protostar. $M_\star$ is calculated according to the method proposed by Tout et al. (1996). The mean $M_\star$ of each group are 2.6±1.6 $M_\odot$, 1.9±0.9 $M_\odot$, and 2.3±1.5 $M_\odot$ respectively. The Hi-GAL source is the parent structure of the protostars, which wraps the protostars, and its luminosity can be regarded as the total luminosity of the protostars. It should be noted that protostars are embedded in cores or clusters, and multiple protostars may be accreting simultaneously (Smith et al. 2009; Cyganowski et al. 2017), but massive protostars are usually much more luminous than low-mass protostars. On the contrary low-mass protostars

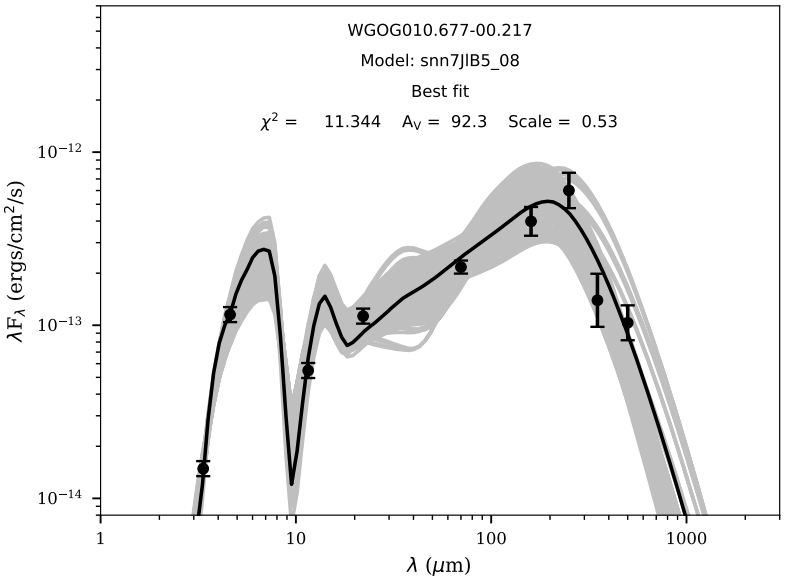


Figure 7. An example of SED fitting. Photometric data from WISE and Hi-GAL were fitted using YSO models of Robitaille (2017). Black and gray lines represent best fit and good fit which satisfy $\chi^2 - \chi^2_{\rm best} < 3N_{\rm data}$, where $N_{\rm data}$ is the numbers of data points. The $P(D \mid M)$ score of this fitting is 4.564.

contribute little for the luminosity. We obtained the median values of $\dot{M}_{\rm acc}$ of each group are 2.04×10^{-4} $M_\odot {\rm yr}^{-1}$, 2.91×10^{-5} $M_\odot {\rm yr}^{-1}$, and 4.22×10^{-5} $M_\odot {\rm yr}^{-1}$, respectively.

4. DISCUSSION

4.1. *The star formation scenario of the WGOs*

Whether a source can be successfully detected depends on its intensity in the direction of sight. 4.5 μm emission of the EGOs identified by Cyganowski et al. (2008) is $\gtrsim 4$ MJy sr^{-1}, and the flux intensity of most of the EGOs in *Spitzer* 4.5 μm band is significantly higher than that in 3.6 μm band (Noriega-Crespo et al. 2004; Cyganowski et al. 2008). We screened 2135 WGOs as young candidates for massive stars, significantly outnumbering *Spitzer* EGOs, which benefits from WISE being twice as sensitive as *Spitzer* (Benjamin et al. 2003; Wright et al. 2010), even though they are filtered by multiple thresholds we set. The empirical relationship between the star formation rate (SFR) in our galaxy and the physical properties of interstellar gas is known as "Kennicutt–Schmidt law": $\Sigma_{\rm SFR} \propto \Sigma^N_{\rm gas}$. This relation states that the SFR is positively related to gas density with the index of the power-law being $\sim$2 in the solar neighborhood (Schmidt 1959) and 1.4 in a larger set of galaxies (Kennicutt & Evans 2012). Cold dust view reveals the confined dust lane in the Galactic Plane, which is bright in -48° $< l <$ 40°, but outside this range gets weaker significantly (Csengeri et al. 2016). WGOs are mainly distributed in $\mid l \mid <$ 60°, which are synergistic with the gas in the plane of the Milky Way. The central molecular zone (CMZ, the inner $\pm$1.5° $\times$ $\pm$0.5° around the Galactic center) contains $\sim$ 10% of neutral gas of Galaxy ($\sim 5 - 10 \times 10^7$ $M_\odot$) (Barnes et al. 2017), but only accounts for 0.1% of the surface area. CMZ has a large amount of dense molecular gas, however due to the extreme environment in this region, its star formation efficiency is very low, only $\sim 0.07 - 0.15$ $M_\odot {\rm yr}^{-1}$ (Crocker et al. 2011; Yusef-Zadeh et al. 2009; An et al. 2011). At the same time, it lacks YSOs with high mass and low mass (total mass of YSOs in the CMZ are $\sim 7.7 \times 10^4$ $M_\odot$) (Immer et al. 2012). The number of our WGO samples is lack in the CMZ, which is consistent with the low SFR in this region.

According to the classification method of the WGOs, Group 1 WGOs are most in line with the morphological characteristics of traditional EGOs (Cyganowski et al. 2008; Chen et al. 2013). The Group 2 WGOs lack the extended structures but show compact green features. The Group 3 WGOs have neither extended structure nor green features, but W2 is 4.5 times larger than W1. The resolution of WISE is about three times lower than that of *Spitzer*, so extended structures of some WGOs may be not identified and are classified into the Group 2 or 3. WGOs in the Groups 2 and 3 do not exhibit extended structures, they show relatively strong W2 band emissions and are usually

surrounded by dense gas, and they may be in an earlier stage (e.g., Class I even Class 0 of YSO, Bachiller 1996; Shu et al. 1987) than the Group 1 and are currently accreting gas.

Molecular tracers behave differently through the evolutionary sequence, and the late evolutionary sequence may contain more complex molecular tracers (Sanhueza et al. 2012). Different masers usually indicate different evolution stages of YSOs, and the star-forming regions with later evolution stages show more complex maser components (e.g., Wang et al. 2011). Class I methanol masers excited by the shock waves are usually found at some distance from a radiation source (Sobolev et al. 2007). It is worth noting that it may occur at the earliest stage, earlier than all masers (Cragg et al. 1992; Ellingsen 2006). Class II methanol masers are widely considered to be one of the most reliable tracers in the early stage of high-mass star formation (Ellingsen 2006, and references therein), and this maser are only related to high-mass star formation activities (Breen et al. 2013). We speculate that the WGOs of Group 1 are in the latest evolutionary stage compared to the other two groups, and the shock wave excited by the strong star formation activity that even excited them near the radiation source leads to the highest association rate with Class I maser near the radiation source. The inference about the evolution stage of Group 1 can also be deduced by observing the association rate of the OH maser: the OH maser is a sensitive tracer of Ultra-Compact H II (UC H II) region (Reid 2002), and the occurred of UC H II region indicates a later stage of star formation. Several previous studies have shown that water maser in star-forming regions can be excited by a variety of star-forming activities (e.g., Hollenbach et al. 2013; Mac Low et al. 1994; Gallimore et al. 2003), and it is obvious that various activities occurring with the process of evolution will improve the excitation rate of water master. The SiO maser have been known associated with late-type stars, such as stars on the AGB (Matsuura et al. 2000; Nakashima & Deguchi 2000). The SiO maser were confirmed that it in star-forming regions is a rare phenomenon by Zapata et al. (2009) as it was only detected from known regions (e.g., Orion KL, Snyder & Buhl 1974; W51 North, Sgr B2, Hasegawa et al. 1986; Sgr B2(N), Higuchi et al. 2015; G19.61-0.23 and G75.78+0.34, Cho et al. 2016). This also leads to the fact that in Fig. 6a, SiO maser appears to be almost unassociated with any WGOs.

4.2. *How many WGOs are high reliable MYSOs?*

The extended structure of the EGOs is likely to be related to the molecular outflow resulting from the shock emission from the molecules H_2 and CO during the formation of a massive star (Cyganowski et al. 2008; Chen et al. 2013). The WISE 4.6 μm is very close to Spitzer's 4.5 μm, and we believe that the extended structure traced by WISE 4.6 μm is also due to the outflow. Outflow is observed toward both low-mass (e.g., famous well researched Herbig–Haro object HH46/47, Noriega-Crespo et al. 2004; Velusamy et al. 2007) and high-mass sources. Strong outflow is one feature of MYSOs. Compared to the flux rate of low-mass outflow $\sim 10^{-6} M_{\odot}\mathrm{yr}^{-1}$, the flux rate of MYSOs can be stronger than $10^{-3} M_{\odot}\mathrm{yr}^{-1}$ (Arce et al. 2007). The bright emission in the W2, which maybe a precursor to a strong outflow in future evolution. However, it cannot be ruled out that there is not enough gas in the parent structure to provide enough gas for it to evolve into a massive star. Thanks to the multi-band SED models for YSOs, we can predict the evolution of the sources and provide us with a way to get more believable subsamples (Robitaille et al. 2006; Robitaille 2017). Massive stars form in clusters (Lada & Lada 2003; Kruijssen 2012), there may be multiple YSOs for one WGO (e.g., MM1∼19 in EGO11.92-0.61, Cyganowski et al. 2017). Limited by the resolution of the WISE, it's indistinguishable. But the massive YSOs have a strong gravitational advantage that will limit the mass of other YSOs in the cluster, once them formed, would dissipate the natal cloud, preventing further star formation (e.g., Herbig 1962). Meanwhile, the luminosity and accretion rate of the massive YSOs are far higher than those of other low-mass YSOs (Arce et al. 2007; Hosokawa et al. 2010).

We selected the WGOs with $M_{\star} + \dot{M}_{\rm acc} \times 10^4$ yr $> 8\ M_{\odot}$ (see blue area in Fig. 8) as robust MYSO candidates, which are listed in Table 2 and the numbers in each group are 46, 118, and 67. The accretion rate changes dramatically during massive star formation, but considering the accretion time scale is usually shorter than 10^4 years, it is generally believed that the accretion rate of MYSOs is $\sim 10^{-4} - 10^{-3}\ M_{\odot}\mathrm{yr}^{-1}$ (Zhang & Tan 2011). We selected WGOs with $\dot{M}_{\rm acc} > 10^{-4}\ M_{\odot}\mathrm{yr}^{-1}$ (see Fig. 8 yellow area) as candidate MYSOs. Table 3 lists those candidate MYSOs. The numbers in each group are 32, 110, and 30. 63% WGOs in Group 1 are robust or candidate MYSOs, much higher than the ratio in Group 2 and 3 (34% and 40%). This probably implies that the WGOs Group 1 have the greatest potential to form massive stars. By observing Fig. 8, we found that almost all stellar mass of MYSO candidates are higher than 1 $M_{\odot}$. Based on the relation of masses and radii of the Hi-GAL sources, we inferred whether massive stars will form. Prestellar and starless cores are separated by the three dotted green lines $\Sigma_{\rm crit} = 0.024$ g cm^{-2} (Lada et al. 2010), $\Sigma_{\rm crit} = 0.027$ g cm^{-2} (Heiderman et al. 2010) and $M(r) = 460 M_{\odot}(r/\mathrm{pc})^{1.9}$ (Larson 1981) in Fig. 9,

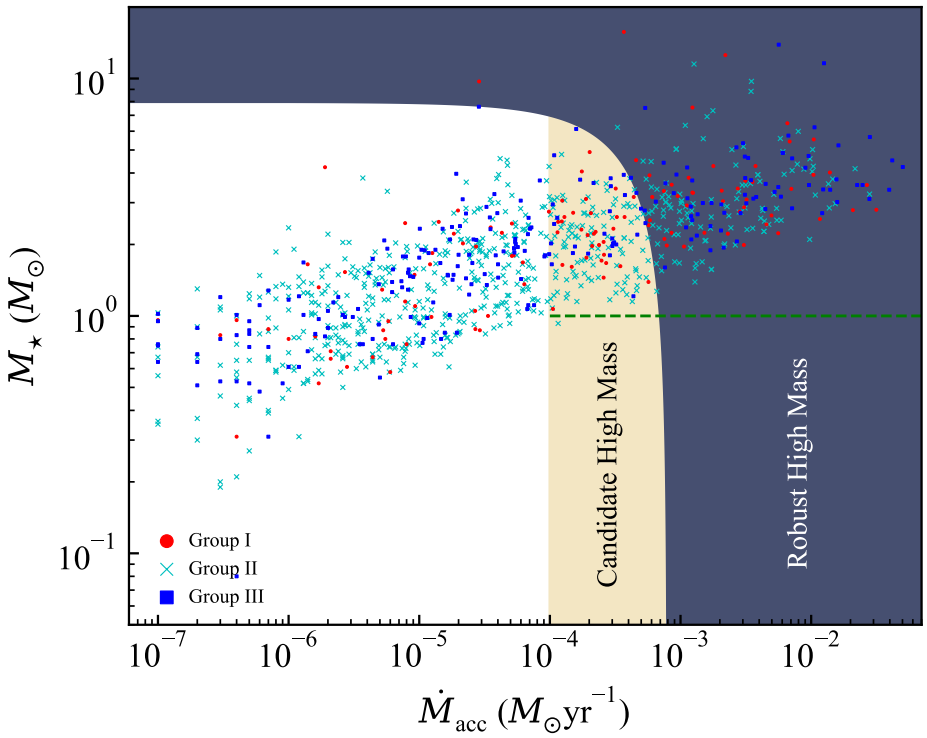


Figure 8. Accretion rate versus protostellar mass. Red circles, blue squares, and cyan crosses represent WGOs in groups 1, 2, and 3, respectively. The WGOs listed in table 2 and 3 are located in the deep blue and light yellow areas, respectively. The green dotted line marks the mass equal to 1 $M_\odot$, and almost all MYSO candidates are above this line.

and the green area means the core in which is not bound by gravity may disperse after a period of time, so the probability of forming stars is very low. Only few WGOs' Hi-GAL source counterparts are under this line, therefore, we can infer that most WGOs' Hi-GAL source counterparts can produce star forming activity. The upper shaded region in Fig. 9 indicates the parameter space of massive protoclusters, defined by Bressert et al. (2012), where there is almost no WGO distribution. Based on theoretical arguments, Krumholz & McKee (2008) establishs a critical value of $\Sigma_{\rm crit} = 1$ g cm^{-2} ($M(r) = \pi\Sigma_{\rm crit} r^2$, dash-dotted yellow line in Fig. 9), but Butler & Tan (2012) and López-Sepulcre et al. (2010) obtained a smaller value of $\Sigma_{\rm crit} = 0.3$ g cm^{-2}. Kauffmann & Pillai (2010) propose an empirical threshold $M(r) \geqslant 870\ M_\odot (r/{\rm pc})^{1.33}$ (dashed red line) as a minimum condition for massive star formation.

Columns (9) and (10) in Table 2 and 3 mark whether robust or candidate MYSOs are greater than thresholds of $M(r) = 870\ M_\odot (r/{\rm pc})^{1.33}$ (hereafter threshold one) and $\Sigma_{\rm crit} = 1$ g/cm^2 (hereafter threshold two). Robust and candidate MYSOs almost all both exceed the threshold one but show significant differences under the threshold two criteria. About 36.7% of candidate MYSOs do not meet threshold two, but this proportion is only 22.5% of robust MYSOs. However, this ratio was significantly increased among non MYSO candidates, and nearly 60% of them did not exceed the threshold two. We infer that the reason for this difference in the ratios is that higher density gas may provide higher accretion just like robust MYSOs, and lower gas mass and density are also difficult to provide larger accretion rate, thus forming MYSOs. Column (11) in Table 2 and 3 is mark that sources whether are associated with Class II methanol maser that is one of the most reliable and sensitive tracers in the early stage of high-mass star formation region (Ellingsen 2006). Nearly 50% of robust MYSOs are associated with Class II methanol maser, and that about 27% of candidate MYSOs, which shows that the former as the MYSOs are more reliable than the latter.

5. CONCLUSIONS

We screened out the WISE objects with green features in the whole Galactic Plane ($0° < l < 360°$ and $-2° < b < 2°$) and selected MYSOs sample with the help of SED fitting from mid-infrared to far-infrared and gravity thresholds. Our findings can be summarized as follows:

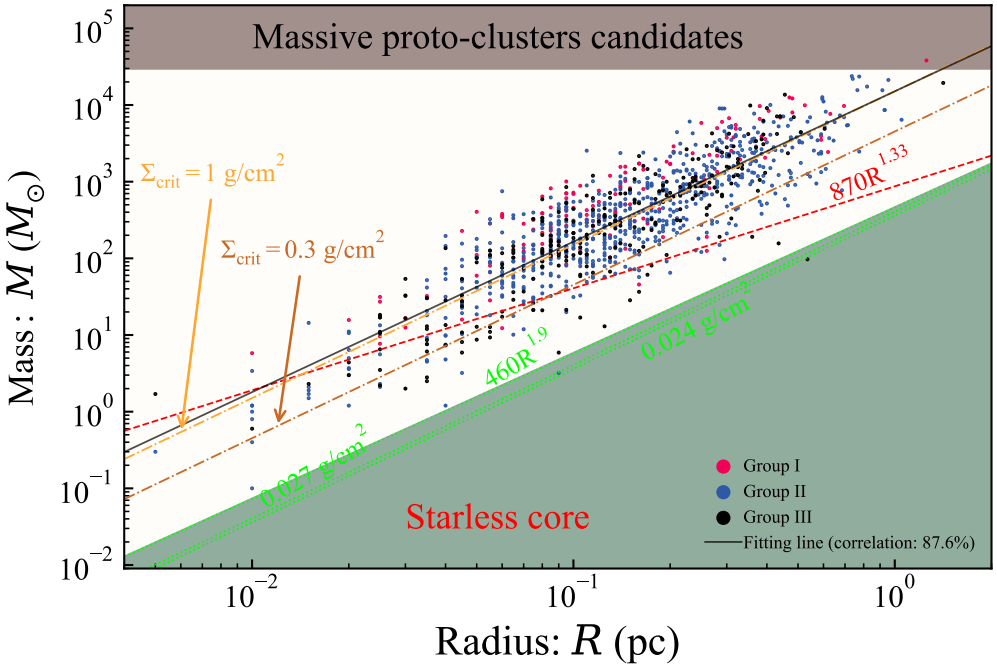


Figure 9. Mass and radius diagram of Hi-GAL compact sources corresponding to WGOs in each group. The black solid line shows a clear correlation between source radius and mass, $\log_{10}(M/M_\odot) = 1.96\log_{10}(R/\mathrm{pc}) + 4.18$. The red dashed line shows the sources which may form high mass star. The yellow dash-dotted indicates another higher threshold ($\Sigma_{\rm crit}$ = 1g/cm^2) for judging high mass clumps. The deep yellow dash-dotted line shows lower threshold than the yellow one.

- After cross-matching with the SIMBAD database to ensure non-YSO exclusions, we identified 2135 WGOs and divided them into three groups. The first group comprises 264 WGOs with an extended green structure, similar to the traditional *Spitzer* EGOs. 1366 WGOs without extended structures but showing compact green features are in the second group. The third group of 505 WGOs is neither extended nor visually green, but numerically W2(green)/W1(blue) is greater than 4.5.

- We find that $\sim$ 75% WGOs are distributed in $\mid l \mid < 60°$, and in $\mid l \mid > 60°$ the distribution of the WGOs is consistent with known star-forming regions. The distribution of WGOs is positively correlated with the density of molecular gas, except in the ultra-dense gas region of the galactic center. The WGOs have a Gaussian distribution along the galactic latitude ($\mid b \mid < 2°$) but shift to negative Galactic latitude by $\sim 0.1°$.

- 1260 WGOs have Hi-GAL source counterparts, accounting for 71% of the total in Hi-GAL survey range. *Spitzer/IRAS* survey catalog shows a high association rate similar to that Hi-GAL catalog, over 54% WGOs matched successfully. However, WISE & 2MASS, RMS, ATLASGAL survey catalog for YSOs show very low association rate with WGOs, 3.2%, 11.1%, 20.8% respectively. By cross-matching with these three catalogs, we obtained 2067, 1635, and 1176 YSOs newly identified and 348 new MYSOs from RMS MYSO sub-catalog.

- The WGOs in Group 1 are in the later evolutionary stage compared to the other two groups, as they have extended structures that is characteristic of outflow and a significantly higher rate of association with various masers, in addition physical parameters such as the luminosity of the parent structure and the gas accretion rate are significantly higher.

- From SED fitting, we obtained the stellar mass $M_\star$ and accretion rate $\dot{M}_{\rm acc}$ of 1151 WGOs. The luminosity of WGOs in goups one is significantly larger than the other two. 231 WGOs with stellar mass $M_\star + \dot{M}_{\rm acc} \times 10^4$ yr $>$ 8 $M_\odot$ are selected as robust MYSOs. 172 WGOs with accretion rate $\dot{M}_{\rm acc} > 10^{-4}$ $M_\odot$yr^{-1} are selected as candidate MYSOs. We find that accretion rate and the density of the parent structure of WGOs are positively correlated.

Table 2. Robust MYSOs

Name	Group	l	b	Model set	Stellar mass ($M_\star$)	Accretion rate ($\dot{M}_{\rm acc}$)	Distance	$\geqslant 870\ M_\odot R^{1.33}$	$\geqslant 1$ g/cm^2	Class II methanol maser
		°	°		$M_\odot$	$\times 10^{-4} M_\odot {\rm yr}^{-1}$	kpc			
(1)	(2)	(3)	(4)	(5)	(6)	(7)	(8)	(9)	(10)	(11)
G000.091-00.663	I	0.0912	-0.6628	s-ubsmi	3.17(0.48)	6.073	8.21	√	√	√
G000.484-00.700	I	0.4837	-0.7003	s-u-smi	15.72(4.83)	3.684	7.32	√	√	
G002.529+00.199	I	2.529	0.199	s-u-hmi	3.71(0.04)	31.305	12.91	√	√	
G004.827+00.231	I	4.827	0.2306	s-pbhmi	2.23(0.0)	55.936	3.62	√	√	
G006.797-00.258	I	6.7968	-0.2581	s-ubsmi	2.56(0.21)	116.692	3.82	√	√	√
G009.779-00.167	I	9.7785	-0.1672	s-u-smi	4.28(3.82)	17.838	11.92	√		
G010.628-00.337	I	10.6281	-0.3369	s-ubhmi	5.43(4.24)	68.455	17.23	√		
G019.008-00.029	I	19.0084	-0.0295	s-ubhmi	2.8(0.58)	315.365	11.67	√	√	√
G019.884-00.535	I	19.8837	-0.5351	s-ubsmi	2.43(0.0)	45.547	3.25	√	√	√
G019.977-00.214	I	19.9773	-0.2141	s-u-smi	2.24(0.81)	8.53	12.35	√	√	
G027.795-00.277	I	27.7951	-0.2771	s-u-smi	2.11(0.69)	7.524	2.94	√	√	
G027.968-00.475	I	27.9676	-0.4746	s-u-smi	1.99(0.53)	30.533	11.82	√	√	
G030.652-00.204	I	30.6516	-0.2042	s-u-hmi	3.67(0.0)	35.535	9.3	√	√	√
G030.788+00.203	I	30.7876	0.2032	s-u-smi	4.53(4.04)	4.568	9.71	√	√	√
G031.580+00.076	I	31.5801	0.0757	s-pbhmi	2.65(0.0)	49.676	4.9	√	√	√
G039.388-00.141	I	39.3877	-0.1414	s-u-smi	2.24(0.0)	15.235	4.0	√	√	√
G039.495-00.993	I	39.4948	-0.993	s-u-hmi	3.57(4.81)	8.559	3.28	√		
G040.278-00.269	I	40.2781	-0.269	s-pbhmi	2.92(2.42)	11.172	8.17	√		√
G045.465+00.043	I	45.4652	0.0431	s-u-smi	3.31(0.66)	12.322	7.08	√	√	
G045.468+00.048	I	45.4678	0.0484	s-u-smi	3.3(0.72)	12.458	7.08	√	√	
G058.468+00.437	I	58.4675	0.4366	s-pbhmi	9.72(18.36)	0.287	4.36	√	√	
G059.783+00.065	I	59.7827	0.0649	s-u-hmi	1.96(0.0)	10.637	2.1	√	√	√
G077.462+01.760	I	77.462	1.7596	s-u-smi	7.55(1.68)	12.341	3.35	√	√	
G311.513-00.454	I	311.5131	-0.4536	s-u-smi	3.2(2.38)	9.513	3.68	√	√	
G313.705-00.190	I	313.7051	-0.1899	s-u-hmi	3.43(1.88)	70.496	8.69	√	√	√
G313.767-00.862	I	313.7668	-0.8625	spu-hmi	3.56(0.0)	267.344	8.08	√	√	√
G316.640-00.087	I	316.6403	-0.0867	s-u-smi	4.28(4.24)	37.478	10.86	√	√	√
G316.959+00.302	I	316.9588	0.3022	s-u-smi	3.93(1.19)	104.254	9.61	√	√	
G317.466-00.403	I	317.4658	-0.4026	s-u-hmi	2.87(0.0)	30.673	9.58	√	√	√
G318.948-00.196	I	318.9476	-0.196	s-ubsmi	12.55(2.68)	22.042	10.38	√	√	√
G320.233-00.284	I	320.2328	-0.2843	s-u-hmi	2.79(0.0)	208.682	8.6	√	√	√
G320.892-00.411	I	320.8923	-0.411	s-u-smi	4.02(0.0)	139.108	10.2	√	√	
G324.716+00.341	I	324.7161	0.3414	s-u-smi	3.36(0.89)	7.448	10.46	√	√	√
G326.544+00.169	I	326.5442	0.1693	spu-hmi	3.09(1.26)	32.043	4.31	√	√	
G326.780-00.241	I	326.78	-0.241	s-pbhmi	3.37(1.63)	20.657	3.83	√	√	
G328.824-00.080	I	328.8237	-0.0798	s-u-smi	3.82(0.0)	11.54	12.08	√		
G330.070+01.063	I	330.07	1.0634	s-ubsmi	6.48(7.74)	65.722	11.78	√	√	√
G332.352-00.117	I	332.3522	-0.1172	s-u-hmi	1.98(0.0)	7.846	3.15	√	√	√
G332.364+00.606	I	332.364	0.6057	s-u-smi	3.44(0.0)	27.394	12.0	√	√	√
G335.060-00.427	I	335.0595	-0.4274	s-pbsmi	2.22(1.42)	23.016	2.72	√	√	√
G337.299-00.874	I	337.2993	-0.8741	s-pbsmi	2.75(0.62)	28.342	10.25	√	√	√
G338.280+00.542	I	338.28	0.5423	s-ubhmi	2.53(0.0)	5.829	3.93	√	√	√
G339.584-00.127	I	339.5838	-0.1273	sp–smi	3.91(2.77)	5.785	12.91	√		√
G339.927-00.083	I	339.9269	-0.0829	s-ubhmi	3.04(0.17)	21.137	3.76	√	√	
G342.705+00.127	I	342.7053	0.1265	s-u-hmi	5.54(0.0)	104.625	12.69	√		
G352.315-00.442	I	352.3155	-0.4421	s-pbhmi	2.41(0.0)	5.698	2.0	√	√	
G000.084-00.642	II	0.084	-0.6417	s-pbhmi	2.34(0.06)	35.679	8.46	√	√	
G000.547-00.851	II	0.5468	-0.8509	s-u-hmi	4.17(0.0)	216.786	7.43	√	√	√
G001.147-00.125	II	1.1468	-0.1247	s-pbsmi	5.59(1.65)	58.091	11.23	√	√	√

Table 2 continued on next page

Table 2 *(continued)*

Name	Group	l	b	Model set	Stellar mass	Accretion rate	Distance	$\geqslant 870\ M_\odot R^{1.33}$	$\geqslant 1$ g/cm^2	Class II
					($M_\star$)	($\dot{M}_{\rm acc}$)				methanol maser
		°	°		$M_\odot$	$\times 10^{-4} M_\odot {\rm yr}^{-1}$	kpc			
(1)	(2)	(3)	(4)	(5)	(6)	(7)	(8)	(9)	(10)	(11)
G007.470+00.057	II	7.4701	0.0575	s-ubhmi	5.17(3.67)	30.284	14.12	√	√	
G007.601-00.139	II	7.6007	-0.139	spu-smi	3.6(0.63)	135.516	8.94	√	√	√
G007.635-00.192	II	7.6347	-0.1923	s-pbhmi	1.78(0.0)	7.134	8.93	√	√	
G008.412-00.346	II	8.4118	-0.3455	s-ubhmi	3.42(1.06)	6.602	12.02	√		
G008.722-00.404	II	8.7219	-0.4036	s-pbsmi	3.49(4.76)	5.982	12.05	√	√	
G010.621-00.443	II	10.6214	-0.4429	s-ubsmi	3.93(0.79)	39.08	16.72	√		
G010.622-00.443	II	10.6221	-0.4434	s-ubsmi	3.93(0.79)	39.08	16.72	√		
G010.724-00.335	II	10.724	-0.3347	s-u-hmi	4.59(2.21)	97.942	16.69	√		√
G011.072-00.386	II	11.0717	-0.3857	s-pbsmi	3.25(2.98)	51.76	16.55	√		
G011.109-00.114	II	11.1089	-0.1143	s-pbsmi	3.26(0.6)	279.858	13.07	√	√	√
G015.665-00.499	II	15.6653	-0.4986	s-u-smi	3.63(0.0)	7.774	14.31	√	√	√
G017.736-00.241	II	17.7356	-0.2409	s-ubhmi	2.85(0.04)	31.171	10.18	√		
G018.262-00.244	II	18.2618	-0.2437	s-u-hmi	2.2(1.15)	9.581	4.51	√	√	√
G018.628-00.070	II	18.6275	-0.0702	s-u-smi	2.01(1.96)	6.678	12.42	√		
G019.611-00.120	II	19.6109	-0.1202	s-ubhmi	2.89(0.95)	22.682	11.77	√	√	
G019.828-00.330	II	19.8284	-0.33	spu-smi	5.02(6.92)	24.731	12.39	√		
G022.356+00.066	II	22.3558	0.0663	spu-smi	2.88(2.8)	10.917	4.85	√	√	√
G023.009-00.411	II	23.0095	-0.4108	s-pbsmi	2.97(2.03)	152.708	4.6	√	√	√
G023.198-00.001	II	23.1977	0.0006	sp–smi	6.35(8.15)	10.881	10.81	√	√	
G023.965-00.110	II	23.9648	-0.1103	s-pbsmi	2.71(0.0)	11.232	4.39	√	√	√
G023.994-00.097	II	23.9944	-0.0973	s-u-smi	6.91(8.765)	15.961	11.0	√	√	
G024.148-00.009	II	24.1483	-0.0092	s-ubsmi	7.32(1.13)	17.691	10.32	√	√	√
G024.427+00.122	II	24.4269	0.1222	s-pbhmi	3.05(0.0)	10.19	9.24	√	√	
G024.427+00.123	II	24.4269	0.1226	s-pbhmi	3.05(0.0)	10.19	9.24	√	√	
G024.541+00.312	II	24.5407	0.3121	s-pbhmi	2.89(1.81)	6.458	5.79	√		√
G024.626-00.101	II	24.6259	-0.1009	s-ubhmi	3.3(2.08)	7.604	9.18	√	√	
G024.731+00.154	II	24.7306	0.1541	s-u-hmi	2.78(0.79)	42.658	5.81	√	√	
G025.710+00.044	II	25.7095	0.0443	s-pbsmi	4.32(3.12)	26.534	10.2	√	√	√
G027.016+00.200	II	27.0162	0.2001	s-u-hmi	2.94(0.15)	8.217	9.74	√	√	
G027.248+00.108	II	27.2476	0.1081	s-ubsmi	1.55(0.23)	7.171	9.87	√		
G028.597-00.021	II	28.5967	-0.0209	sp–smi	6.23(1.95)	3.293	9.14	√		
G028.652+00.027	II	28.6519	0.0268	s-pbsmi	9.73(4.39)	34.893	8.97	√	√	
G028.700+00.406	II	28.6998	0.4063	s-ubsmi	4.49(4.87)	5.17	9.55	√		√
G028.842+00.494	II	28.8424	0.4936	s-pbhmi	3.01(0.0)	7.697	9.89	√	√	√
G030.348+00.392	II	30.3478	0.392	s-pbhmi	2.53(0.0)	54.637	9.24	√	√	
G030.603+00.176	II	30.6035	0.1758	s-u-hmi	3.18(0.0)	8.113	8.45	√	√	
G030.770-00.804	II	30.7696	-0.8044	s-ubsmi	2.27(0.75)	43.502	9.87	√	√	√
G030.770-00.805	II	30.7697	-0.8048	s-ubsmi	2.27(0.75)	43.502	9.87	√	√	√
G030.920+00.088	II	30.9203	0.0878	s-ubhmi	2.59(0.78)	11.419	8.96	√	√	
G030.972-00.142	II	30.9723	-0.1417	s-ubhmi	2.63(0.44)	7.386	4.44	√	√	√
G031.900+00.341	II	31.9003	0.3407	s-u-hmi	1.66(0.7)	13.185	14.06	√		
G032.118+00.090	II	32.1177	0.0903	s-u-hmi	3.34(0.0)	27.84	8.37	√	√	√
G032.992+00.034	II	32.9917	0.034	s-pbsmi	3.56(0.0)	29.694	9.26	√	√	√
G033.229-00.018	II	33.2292	-0.0184	s-u-smi	1.99(0.0)	26.258	8.02	√	√	√
G033.393+00.010	II	33.3927	0.0096	s-pbhmi	3.02(0.13)	7.732	7.83	√	√	√
G035.148+00.809	II	35.1484	0.8091	s-pbsmi	2.01(0.0)	21.779	9.29	√	√	√
G035.417-00.285	II	35.4167	-0.2846	s-pbhmi	2.1(0.0)	97.352	10.46	√	√	
G037.769-00.393	II	37.769	-0.3925	s-ubhmi	2.29(0.71)	7.821	12.33	√		
G037.874-00.399	II	37.8736	-0.3991	s-u-hmi	8.83(5.21)	34.673	9.45	√	√	
G038.120-00.228	II	38.1195	-0.2279	s-pbhmi	2.74(0.0)	28.125	5.24	√	√	√
G038.933-00.361	II	38.9331	-0.3607	s-u-hmi	2.85(1.41)	8.434	10.48	√	√	

Table 2 continued on next page

Table 2 *(continued)*

Name	Group	l	b	Model set	Stellar mass	Accretion rate	Distance	$\geqslant 870\ M_\odot R^{1.33}$	$\geqslant 1$ g/cm^2	Class II
					($M_\star$)	($\dot{M}_{\rm acc}$)				methanol maser
		°	°		$M_\odot$	$\times 10^{-4} M_\odot {\rm yr}^{-1}$	kpc			
(1)	(2)	(3)	(4)	(5)	(6)	(7)	(8)	(9)	(10)	(11)
G039.100+00.491	II	39.0999	0.4909	s-ubhmi	2.73(0.0)	28.917	11.48	√	√	√
G041.307-00.169	II	41.3067	-0.1693	s-pbhmi	1.98(0.0)	21.493	8.96	√		√
G043.037-00.451	II	43.0374	-0.4512	s-ubsmi	4.1(3.88)	71.495	8.5	√	√	√
G043.074-00.077	II	43.0742	-0.0775	s-u-hmi	1.69(0.0)	14.642	11.32	√	√	√
G043.177-00.518	II	43.1771	-0.5185	s-pbsmi	3.61(0.3)	34.346	8.46	√	√	√
G048.364+00.247	II	48.3635	0.2469	s-ubsmi	1.59(0.13)	12.945	10.66	√		
G048.856+00.235	II	48.8556	0.2351	s-ubhmi	2.98(0.65)	10.104	9.9	√		
G050.033+00.581	II	50.0335	0.5811	s-u-smi	3.12(0.25)	26.955	10.85	√	√	√
G054.110-00.081	II	54.1097	-0.0812	s-ubsmi	2.61(1.75)	17.184	4.3	√	√	
G071.312+00.828	II	71.3124	0.8278	spu-hmi	3.95(3.8)	62.095	4.08	√	√	
G111.859+00.801	II	111.8595	0.8013	s-u-hmi	2.34(0.0)	16.961	3.2	√	√	
G286.727-00.194	II	286.7271	-0.1942	s-pbsmi	2.45(0.0)	12.148	6.32	√	√	
G297.140-01.341	II	297.14	-1.3406	s-u-smi	2.97(3.05)	12.469	9.07	√		
G297.403-00.652	II	297.4026	-0.6515	s-pbsmi	2.53(0.05)	10.158	10.01	√		
G298.723-00.086	II	298.7231	-0.0861	s-pbsmi	2.45(0.0)	9.799	4.01	√	√	√
G311.567+00.319	II	311.5671	0.3186	sp–hmi	2.95(1.8)	20.972	7.65	√	√	
G311.627+00.290	II	311.6269	0.29	s-ubsmi	3.77(1.29)	5.461	6.88	√	√	√
G311.629+00.266	II	311.6286	0.2655	s-ubhmi	3.26(3.16)	9.879	4.64	√	√	√
G311.947+00.142	II	311.9467	0.1417	s-u-hmi	2.79(0.0)	7.407	8.29	√	√	√
G312.412-01.050	II	312.4121	-1.0496	s-u-hmi	2.35(1.24)	6.843	3.14	√	√	
G312.590-00.503	II	312.5899	-0.5027	s-u-hmi	2.64(0.0)	23.437	6.79	√		
G313.469+00.190	II	313.4692	0.1904	spu-smi	5.02(5.75)	102.515	11.01	√	√	√
G314.239+00.365	II	314.2387	0.3653	s-ubsmi	2.76(1.83)	9.824	6.7	√		
G317.028+00.361	II	317.0283	0.3613	spu-smi	2.77(0.23)	12.177	9.03	√		√
G319.178-00.409	II	319.1783	-0.4085	spu-hmi	4.92(5.33)	60.745	10.93	√		
G326.268-00.486	II	326.2685	-0.4858	s-pbhmi	4.06(3.1)	101.904	10.31	√	√	
G326.279+00.561	II	326.2787	0.5612	s-u-smi	1.66(0.0)	6.539	11.19	√		
G326.322-00.395	II	326.3222	-0.3953	s-pbhmi	2.53(0.0)	58.885	9.69	√	√	√
G326.795+00.382	II	326.7951	0.3822	s-u-hmi	3.69(0.0)	40.486	12.53	√	√	
G329.466+00.516	II	329.4664	0.5157	sp–hmi	3.16(0.46)	7.236	10.42	√	√	
G329.717+00.804	II	329.7174	0.8038	s-pbhmi	1.39(0.09)	12.89	11.32	√	√	
G329.719+01.164	II	329.7189	1.1638	s-ubsmi	2.07(0.0)	15.379	4.45	√	√	√
G330.026+01.043	II	330.0258	1.0428	s-ubsmi	1.69(0.0)	9.026	11.49	√	√	
G330.035+01.045	II	330.035	1.0446	s-ubhmi	1.67(0.52)	9.785	11.47	√	√	
G331.119-00.118	II	331.1191	-0.1181	s-ubsmi	2.37(0.54)	14.238	9.79	√		√
G331.342-00.346	II	331.3415	-0.3462	s-ubsmi	11.51(3.73)	12.684	3.88	√	√	√
G331.491-00.116	II	331.491	-0.1157	s-pbhmi	2.84(1.39)	54.36	4.82	√	√	
G332.583+00.147	II	332.5827	0.1473	s-pbsmi	2.76(1.76)	6.042	11.89	√	√	√
G332.942-00.686	II	332.9415	-0.6863	s-ubsmi	4.47(4.45)	5.961	3.8	√	√	
G333.184-00.091	II	333.1838	-0.0907	s-ubsmi	2.08(0.0)	15.636	4.85	√	√	√
G336.410-00.255	II	336.4102	-0.2554	s-u-hmi	5.99(5.49)	79.671	10.34	√	√	√
G336.432-00.262	II	336.4325	-0.2616	s-pbhmi	2.85(0.68)	137.634	10.22	√	√	√
G336.871+00.295	II	336.8706	0.2954	s-u-hmi	1.57(0.0)	17.249	11.21	√	√	
G336.941-00.156	II	336.9405	-0.1562	s-ubsmi	3.23(0.64)	107.585	10.96	√	√	√
G336.958-00.977	II	336.9578	-0.9771	s-ubhmi	3.56(0.68)	31.592	12.22	√	√	√
G337.686+00.138	II	337.6859	0.1382	s-pbhmi	2.58(1.18)	41.125	11.01	√	√	√
G338.140+00.178	II	338.1396	0.1783	s-ubsmi	2.51(1.3)	43.855	13.02	√	√	√
G338.392-00.403	II	338.3916	-0.4029	spu-smi	4.15(2.25)	87.926	12.72	√	√	√
G338.472+00.289	II	338.4718	0.2887	s-pbsmi	2.2(1.29)	8.928	2.37	√	√	√
G339.948-00.539	II	339.9484	-0.5389	s-ubsmi	2.84(0.0)	42.258	5.32	√	√	√
G341.215-00.236	II	341.2152	-0.2358	s-u-hmi	5.58(2.35)	14.925	3.45	√	√	

Table 2 continued on next page

Table 2 *(continued)*

Name	Group	l	b	Model set	Stellar mass	Accretion rate	Distance	$\geqslant 870\ M_\odot R^{1.33}$	$\geqslant 1$ g/cm^2	Class II
					($M_\star$)	($\dot{M}_{\rm acc}$)				methanol maser
		°	°		$M_\odot$	$\times 10^{-4} M_\odot {\rm yr}^{-1}$	kpc			
(1)	(2)	(3)	(4)	(5)	(6)	(7)	(8)	(9)	(10)	(11)
G341.218-00.213	II	341.2178	-0.2127	spu-smi	2.43(0.89)	47.365	3.37	√	√	√
G342.905-00.120	II	342.9048	-0.1202	s-pbhmi	2.41(0.0)	6.136	5.25	√	√	
G343.444-00.203	II	343.444	-0.2032	s-ubsmi	2.31(1.35)	32.268	16.36	√		
G344.065+00.114	II	344.0655	0.1135	s-u-hmi	2.71(0.88)	5.7	11.47	√		
G345.985-00.020	II	345.9847	-0.0205	s-u-smi	3.09(0.04)	17.216	10.81	√	√	√
G346.369-00.647	II	346.3686	-0.6471	s-u-hmi	1.93(0.0)	11.93	17.06	√		
G347.817+00.018	II	347.8168	0.0177	s-u-hmi	1.57(0.0)	17.244	13.06	√	√	√
G350.105+00.080	II	350.1047	0.0804	s-pbhmi	5.06(5.25)	9.29	5.6	√	√	
G352.161+00.199	II	352.1612	0.1992	spu-hmi	2.35(0.4)	24.291	11.55	√	√	
G357.553-00.548	II	357.553	-0.5477	s-pbhmi	4.27(0.0)	103.827	17.11	√		
G357.609-00.618	II	357.6093	-0.618	s-u-hmi	4.36(1.59)	78.327	18.9	√		
G357.966-00.163	II	357.9664	-0.1634	sp–smi	5.03(0.67)	9.241	13.95	√	√	√
G359.436-00.102	II	359.4363	-0.1018	s-u-hmi	3.77(0.0)	146.105	8.62	√	√	√
G007.333-00.016	III	7.3335	-0.0163	spu-smi	2.95(1.69)	20.539	13.21	√	√	
G010.575-00.577	III	10.5749	-0.5771	s-ubsmi	5.67(9.27)	281.369	16.4	√	√	
G010.824-00.103	III	10.8238	-0.1031	s-u-smi	3.17(0.67)	37.947	11.0	√		√
G011.116+00.051	III	11.1156	0.0514	s-u-smi	5.34(6.54)	30.111	13.48	√	√	
G011.992-00.272	III	11.9917	-0.2722	s-pbhmi	3.18(0.0)	58.651	11.44	√	√	√
G012.025-00.032	III	12.0252	-0.0316	s-u-smi	3.4(2.12)	139.828	9.4	√	√	√
G012.158-00.134	III	12.1583	-0.1343	s-ubhmi	3.56(0.0)	247.357	16.2	√		
G012.199-00.034	III	12.1986	-0.0342	s-pbhmi	4.72(0.0)	95.534	11.81	√	√	√
G012.525+00.016	III	12.5255	0.0158	s-ubhmi	3.56(1.51)	96.208	12.84	√	√	√
G013.184-00.107	III	13.1836	-0.1068	spu-smi	2.63(3.9)	12.041	4.45	√	√	
G013.210-00.143	III	13.2102	-0.1434	s-u-smi	2.72(1.23)	21.64	4.46	√	√	
G013.713-00.084	III	13.7127	-0.0837	s-u-hmi	1.89(0.3)	16.938	4.05	√	√	√
G014.949-00.072	III	14.9493	-0.0722	s-pbsmi	2.68(0.0)	13.509	11.15	√	√	
G017.964+00.080	III	17.9643	0.08	s-u-smi	13.89(6.63)	56.429	13.84	√	√	
G018.296+00.429	III	18.2964	0.4294	s-ubsmi	2.18(0.0)	13.326	15.68			
G020.239+00.065	III	20.2387	0.0649	s-pbhmi	2.1(0.0)	12.094	4.43	√	√	√
G023.818+00.384	III	23.8176	0.3836	spu-hmi	4.63(5.1)	32.933	10.76	√		
G024.442-00.228	III	24.4424	-0.2282	s-u-smi	2.06(0.47)	26.987	3.69	√	√	
G025.398+00.562	III	25.3979	0.5618	s-pbsmi	3.6(0.0)	44.832	13.75	√	√	
G025.613-00.137	III	25.613	-0.1366	s-u-hmi	3.73(2.1)	34.695	9.87	√	√	
G026.496+00.711	III	26.4956	0.7105	s-u-smi	4.21(1.0)	90.278	11.85	√	√	
G029.319-00.162	III	29.3195	-0.1617	s-ubhmi	3.12(0.33)	36.091	11.59	√	√	√
G030.463+00.032	III	30.4633	0.0324	s-pbsmi	3.81(2.91)	31.274	8.42	√	√	
G030.588-00.043	III	30.5883	-0.0427	s-u-smi	5.23(0.0)	161.709	11.71	√	√	√
G030.866+00.114	III	30.866	0.1144	s-u-smi	5.75(4.27)	66.956	11.9	√	√	
G030.958+00.087	III	30.958	0.0866	s-u-hmi	4.24(2.08)	502.697	11.76	√	√	√
G030.972+00.562	III	30.9723	0.5622	s-pbsmi	3.02(0.29)	158.286	12.72	√		√
G030.980+00.216	III	30.9797	0.2156	s-ubhmi	4.42(5.81)	7.426	8.07	√	√	√
G034.756+00.025	III	34.7563	0.0245	s-u-hmi	3.62(3.93)	7.669	4.43	√	√	√
G036.878-00.473	III	36.8777	-0.4729	s-u-hmi	2.39(0.54)	16.941	3.66	√	√	
G040.282-00.220	III	40.2816	-0.2196	s-pbhmi	2.71(0.0)	121.499	4.71	√	√	√
G041.132+00.129	III	41.132	0.1291	spu-smi	2.98(1.98)	31.889	8.76	√		
G042.098+00.352	III	42.0982	0.3517	spu-hmi	3.76(2.19)	156.175	11.04	√	√	
G043.306-00.211	III	43.3065	-0.2108	s-u-hmi	2.29(0.0)	20.407	3.84	√	√	
G049.043-01.079	III	49.043	-1.0786	s-pbhmi	5.13(5.95)	26.783	8.2	√	√	√
G049.265+00.311	III	49.2649	0.3108	s-pbhmi	3.49(0.0)	56.019	10.67	√	√	√
G049.544-00.883	III	49.5435	-0.8831	s-u-hmi	2.71(0.0)	28.815	7.73	√		
G050.779+00.152	III	50.7786	0.1518	spu-hmi	3.29(4.84)	8.88	7.42	√	√	√

Table 2 continued on next page

Table 2 *(continued)*

Name	Group	l	b	Model set	Stellar mass ($M_\star$)	Accretion rate ($\dot{M}_{\rm acc}$)	Distance	$\geqslant 870\ M_\odot R^{1.33}$	$\geqslant 1$ g/cm^2	Class II methanol maser
		°	°		$M_\odot$	$\times 10^{-4} M_\odot {\rm yr}^{-1}$	kpc			
(1)	(2)	(3)	(4)	(5)	(6)	(7)	(8)	(9)	(10)	(11)
G052.844-00.868	III	52.8438	-0.8675	s-u-smi	3.94(4.33)	9.306	6.25	√		
G288.962+00.265	III	288.962	0.2645	s-u-smi	3.72(3.86)	12.297	6.23	√	√	
G289.944-00.891	III	289.9441	-0.8907	spu-smi	11.6(2.01)	125.42	8.57	√	√	
G304.665-00.965	III	304.6652	-0.9651	s-ubhmi	3.56(0.11)	224.894	9.77	√	√	
G305.475-00.096	III	305.4749	-0.0962	s-pbsmi	2.89(0.0)	11.977	6.54	√	√	√
G312.097-00.236	III	312.0971	-0.2359	s-u-hmi	3.33(1.5)	52.489	8.09	√		
G318.471-00.214	III	318.4714	-0.2141	s-ubsmi	2.53(0.84)	12.298	10.01	√	√	√
G319.323-00.135	III	319.323	-0.1349	s-ubhmi	2.99(0.0)	17.285	11.15	√	√	
G320.360-00.282	III	320.3597	-0.2816	s-pbhmi	1.6(0.0)	7.6	8.7	√	√	
G320.517-00.340	III	320.5169	-0.3397	s-ubhmi	3.03(2.44)	6.47	8.71	√		
G324.923-00.568	III	324.9233	-0.5682	s-ubsmi	2.99(0.0)	14.821	4.4	√	√	√
G327.119+00.511	III	327.1195	0.5108	s-u-smi	3.11(0.0)	279.123	4.96	√	√	√
G327.402+00.445	III	327.402	0.4449	s-pbsmi	2.78(0.0)	5.324	4.63	√	√	√
G327.654+00.126	III	327.6537	0.1255	s-u-hmi	2.36(0.0)	11.033	5.16	√	√	
G328.164+00.587	III	328.1644	0.5868	s-u-smi	3.24(0.0)	31.103	8.98	√	√	√
G329.066-00.308	III	329.066	-0.3079	s-pbhmi	6.23(7.12)	106.091	11.62	√	√	√
G331.710+00.603	III	331.7095	0.603	s-u-smi	1.94(0.0)	21.389	4.05	√	√	√
G333.314+00.105	III	333.3145	0.1051	s-pbhmi	4.86(0.0)	60.606	11.94	√	√	√
G333.315+00.105	III	333.3146	0.1054	s-pbhmi	4.86(0.0)	60.606	11.94	√	√	√
G337.052-00.226	III	337.052	-0.2259	s-u-smi	2.84(0.56)	71.454	10.86	√		√
G338.000-00.149	III	337.9999	-0.1494	s-u-smi	3.4(0.46)	395.611	11.33	√		
G339.621-00.121	III	339.6212	-0.1206	s-u-hmi	2.82(0.0)	44.576	2.6	√	√	√
G339.986-00.425	III	339.9863	-0.4247	s-u-hmi	4.22(0.0)	11.245	10.53	√		√
G340.248-00.372	III	340.2483	-0.3717	s-u-hmi	4.69(0.0)	31.053	11.99	√	√	√
G342.958-00.318	III	342.9584	-0.3177	sp–smi	4.61(4.21)	71.55	12.7	√	√	
G344.915-00.229	III	344.9149	-0.2291	s-ubsmi	7.52(5.63)	5.367	10.72	√	√	
G349.883+00.231	III	349.8834	0.2306	s-u-hmi	4.52(1.89)	417.632	21.77	√		√
G356.662-00.264	III	356.662	-0.2641	spu-hmi	3.41(2.04)	123.559	6.75	√	√	√
G357.169-00.916	III	357.1692	-0.9159	sp–smi	3.13(0.87)	11.291	19.56	√		

NOTE—Catalog of WGOs as robust MYSOs. Column (1): source name (Galactic coordinate); Column (2): group; Column (3) and (4): Galactic coordinate (longitude: l, latitude: b) of the 4.6 μm emission; Column (5): name of beat-fit model set; Column (6): protostellar mass estimated according to the method provided by Tout et al. (1996), uncertainty in brackets is obtained by error propagation; Column (7): accretion rate obtained from SED fitting (Robitaille 2017); Column (8): distance obtained from Elia et al. (2021); Column (9)-(10): thresholds indicating whether a source can form massive stars, and high-mass sources are marked with "√"; Column (11): Class II methanol maser, and if the source is associated with it, then marked with "√".

Table 3. Candidate MYSOs

Name	Group	l	b	Model set	Stellar mass ($M_\star$)	Accretion rate ($\dot{M}_{\rm acc}$)	Distance	$\geqslant 870\ M_\odot R^{1.33}$	$\geqslant 1$ g/cm^2	Class II methanol maser
		°	°		$M_\odot$	$\times 10^{-4} M_\odot {\rm yr}^{-1}$	kpc			
(1)	(2)	(3)	(4)	(5)	(6)	(7)	(8)	(9)	(10)	(11)
G001.934-00.170	I	1.9344	-0.1699	s-pbhmi	2.61(0.12)	3.256	10.09	√		
G008.683-00.368	I	8.6833	-0.3678	s-u-hmi	3.11(0.0)	1.89	4.19	√	√	√
G010.477-00.358	I	10.4768	-0.3584	s-u-smi	1.39(0.53)	5.681	17.1	√	√	
G011.918-00.613	I	11.9181	-0.6131	s—smi	3.06(1.44)	1.243	3.4	√	√	
G012.683-00.183	I	12.6827	-0.1829	s-pbsmi	2.72(1.73)	1.507	2.4	√	√	√
G012.890+00.491	I	12.8904	0.4915	s-pbhmi	1.76(0.31)	1.904	2.3	√	√	√
G028.832-00.252	I	28.832	-0.2522	s-u-smi	3.17(0.32)	4.383	4.86	√	√	√
G035.133-00.745	I	35.1326	-0.745	s-u-hmi	2.05(0.0)	2.578	2.08	√	√	√

Table 3 continued on next page

Table 3 *(continued)*

Name	Group	l	b	Model set	Stellar mass	Accretion rate	Distance	$\geqslant 870\ M_\odot R^{1.33}$	$\geqslant 1$ g/cm^2	Class II
					($M_\star$)	($\dot{M}_{\rm acc}$)				methanol maser
		$^\circ$	$^\circ$		$M_\odot$	$\times 10^{-4} M_\odot {\rm yr}^{-1}$	kpc			
(1)	(2)	(3)	(4)	(5)	(6)	(7)	(8)	(9)	(10)	(11)
G037.042-00.033	I	37.0418	-0.0334	s-u-hmi	2.61(0.04)	3.731	4.93	√	√	
G058.774+00.645	I	58.7738	0.6449	s-u-smi	2.49(1.71)	1.156	3.3	√	√	√
G083.465+00.157	I	83.4647	0.1574	s-ubhmi	1.97(1.27)	2.106	2.88	√		
G111.877+00.996	I	111.8773	0.9956	s-ubhmi	2.25(2.46)	1.144	3.2	√	√	
G294.512-01.620	I	294.5117	-1.6205	spu-hmi	2.33(1.89)	3.063	2.2	√	√	√
G305.536+00.942	I	305.5358	0.942	s-u-hmi	1.07(0.33)	1.055	7.66	√	√	
G309.535-00.739	I	309.5347	-0.7389	s-ubsmi	4.06(3.58)	1.756	4.58	√	√	
G312.108+00.262	I	312.1084	0.2623	s-ubhmi	1.81(0.26)	2.596	3.69	√	√	√
G320.184+00.840	I	320.184	0.8399	s-pbhmi	1.64(0.38)	1.247	2.48			
G321.936-00.006	I	321.9356	-0.0063	s-u-hmi	1.71(0.0)	2.485	2.13	√	√	
G326.858-00.677	I	326.8583	-0.677	s-u-hmi	1.45(0.0)	2.579	3.87	√	√	√
G329.556+00.178	I	329.5555	0.1781	s-pbsmi	2.19(0.25)	1.945	8.85	√		√
G331.623+00.526	I	331.623	0.5263	s-u-hmi	2.5(0.27)	1.233	3.23	√	√	
G332.122+00.936	I	332.1215	0.9358	s-pbhmi	1.61(0.0)	1.47	4.36	√	√	
G333.076-00.559	I	333.076	-0.559	s-pbsmi	2.31(0.57)	1.743	3.8	√	√	
G333.465-00.163	I	333.4653	-0.163	s-u-hmi	4.9(7.205)	2.016	2.86	√	√	√
G334.332+00.964	I	334.3317	0.964	s-ubsmi	2.61(1.58)	1.292	3.37	√	√	
G335.789+00.174	I	335.7889	0.1743	s-ubsmi	3.44(0.15)	3.191	3.23	√	√	√
G340.970-01.022	I	340.9701	-1.0217	s-pbsmi	2.22(0.28)	2.174	2.0	√	√	√
G341.238-00.271	I	341.2378	-0.2708	s-u-smi	2.71(0.63)	2.06	3.47	√	√	√
G343.501-00.473	I	343.5013	-0.4731	s-u-smi	1.67(0.27)	2.697	2.0	√	√	√
G349.644-01.095	I	349.6436	-1.0953	s-u-hmi	2.26(2.13)	2.239	2.2	√	√	
G081.662+00.551	I	81.6615	0.5506	s-pbsmi	1.99(0.995)	2.377	2.92	√		
G305.193-00.005	I	305.1931	-0.0055	s-pbhmi	1.62(1.11)	3.464	2.85	√	√	
G003.347+00.441	II	3.3465	0.4414	s-u-smi	3.38(1.32)	2.741	11.16	√		
G005.910-00.544	II	5.9095	-0.5442	s-pbhmi	1.54(0.18)	1.115	3.27	√	√	
G006.922-00.251	II	6.9219	-0.2513	s-ubsmi	2.15(0.89)	1.387	3.82	√	√	
G007.993-00.269	II	7.9931	-0.2691	s-u-hmi	3.11(0.0)	3.18	11.79			
G012.903-00.032	II	12.9032	-0.0315	s-u-hmi	2.88(0.57)	4.059	4.7	√	√	√
G013.097-00.145	II	13.0968	-0.1447	s-ubhmi	1.91(0.58)	3.475	4.05	√	√	
G013.280+00.092	II	13.2801	0.0917	s-ubsmi	1.55(0.18)	4.567	13.09	√		
G014.012-00.175	II	14.0118	-0.1754	s-u-hmi	1.45(0.0)	2.346	3.72	√	√	
G014.320-00.133	II	14.3205	-0.1328	s-u-hmi	3.06(2.06)	1.021	12.57	√		
G018.234+00.654	II	18.2342	0.6536	sp–hmi	2.97(0.27)	3.948	12.79	√	√	
G018.246-00.472	II	18.2464	-0.4719	s-u-smi	1.25(0.29)	3.202	12.15	√		
G018.256-00.253	II	18.2565	-0.2527	s-u-hmi	2.86(2.84)	1.058	4.46	√	√	
G018.930+00.083	II	18.9305	0.0829	s-pbhmi	2.39(1.56)	2.592	12.36	√		
G019.365-00.029	II	19.3651	-0.0293	s-pbhmi	2.12(0.42)	3.027	2.22	√	√	√
G020.234+00.084	II	20.234	0.0844	s-u-hmi	1.89(0.33)	5.141	11.12	√	√	
G022.038+00.222	II	22.0381	0.2222	s-pbhmi	2.4(0.0)	1.775	3.43	√	√	√
G023.227+00.163	II	23.2272	0.1629	spu-hmi	1.08(0.17)	1.043	4.59	√		
G023.569+00.011	II	23.5685	0.0109	s-pbhmi	3.07(2.15)	1.298	5.66	√	√	
G024.633+00.153	II	24.6334	0.1528	s-pbsmi	1.36(0.0)	3.268	3.45	√	√	√
G024.639-00.030	II	24.6389	-0.0304	s-ubsmi	2.13(0.48)	5.635	15.99	√		
G024.942+00.074	II	24.9423	0.074	s-ubhmi	1.64(0.0)	2.142	2.81	√	√	
G025.569-00.095	II	25.5689	-0.0953	s-u-smi	1.23(0.0)	3.875	9.85	√		
G025.920-00.141	II	25.92	-0.1408	s-ubhmi	2.59(1.46)	4.678	9.22	√		√
G026.663+00.275	II	26.6631	0.2747	s-u-smi	2.65(0.82)	2.279	8.87	√		
G026.770-00.102	II	26.7703	-0.1025	spu-hmi	1.58(0.31)	4.535	9.53	√		
G027.294-00.156	II	27.2939	-0.156	s-u-smi	1.96(1.98)	1.317	9.8	√		
G027.956+00.114	II	27.956	0.1142	spu-hmi	1.45(0.37)	5.466	13.15	√		

Table 3 continued on next page

Table 3 *(continued)*

Name	Group	l	b	Model set	Stellar mass	Accretion rate	Distance	$\geqslant 870\ M_\odot R^{1.33}$	$\geqslant 1$ g/cm^2	Class II
					($M_\star$)	($\dot{M}_{\rm acc}$)				methanol maser
		°	°		$M_\odot$	$\times 10^{-4} M_\odot {\rm yr}^{-1}$	kpc			
(1)	(2)	(3)	(4)	(5)	(6)	(7)	(8)	(9)	(10)	(11)
G028.320-00.011	II	28.3197	-0.0108	spu-smi	4.79(6.59)	1.229	5.44	√	√	√
G029.277-00.128	II	29.2773	-0.1283	s-u-hmi	2.13(0.0)	3.703	3.63	√	√	√
G029.278-00.128	II	29.2782	-0.1284	s-u-hmi	2.13(0.0)	3.703	3.63	√	√	√
G029.325-00.515	II	29.3246	-0.5146	sp–hmi	2.05(1.0)	1.29	8.94			
G029.363-00.551	II	29.3627	-0.5512	s—smi	2.16(0.3)	2.76	10.74	√		
G029.780-00.260	II	29.7796	-0.2597	s-ubhmi	1.17(0.27)	2.875	8.93	√	√	
G030.300-00.203	II	30.3001	-0.2032	s-u-smi	2.67(2.04)	1.011	8.71	√		√
G030.945+00.157	II	30.9447	0.1573	s-u-hmi	2.17(1.38)	1.562	8.57	√		√
G034.575-00.000	II	34.5746	0.0	s-u-smi	1.15(0.0)	4.275	9.3	√	√	
G034.712-00.644	II	34.7121	-0.6445	sp–smi	2.19(1.31)	1.97	10.86	√		
G034.994-00.045	II	34.9938	-0.0446	s-pbsmi	1.79(1.44)	1.109	10.84	√		
G035.499-00.021	II	35.4989	-0.0208	sp–smi	3.6(3.75)	2.701	10.1	√	√	
G037.359-00.074	II	37.3587	-0.0739	sp–hmi	3.22(3.04)	1.253	10.7	√		
G037.753+00.197	II	37.753	0.1972	s-ubhmi	2.13(1.0)	1.649	10.44	√	√	
G037.763-00.215	II	37.7629	-0.2151	s-ubsmi	2.9(2.38)	4.474	9.58	√	√	
G043.326-00.202	II	43.3258	-0.2025	s-pbsmi	2.36(0.34)	1.217	8.16	√	√	
G044.097+00.160	II	44.0965	0.16	s-ubhmi	1.54(0.81)	1.504	8.31	√	√	
G046.246-00.773	II	46.2464	-0.7735	s-u-hmi	1.27(0.0)	6.582	7.95	√		
G046.871-00.301	II	46.8713	-0.3012	s-u-hmi	1.95(0.15)	1.272	8.63	√		
G049.381-00.184	II	49.3813	-0.184	spu-hmi	2.73(1.63)	2.579	7.25	√		
G050.916-00.722	II	50.9159	-0.7217	s-ubhmi	3.08(2.64)	1.082	7.7	√		
G052.341+00.324	II	52.3408	0.3242	s-ubhmi	1.38(0.42)	3.745	6.26	√		
G054.371-00.613	II	54.3709	-0.6132	s-pbsmi	2.29(0.0)	1.399	7.3	√	√	√
G060.621-00.700	II	60.621	-0.6997	s-u-hmi	1.29(0.21)	3.612	5.05	√		
G063.115+00.341	II	63.1148	0.3414	s-ubsmi	2.38(0.33)	1.433	2.2	√	√	
G074.569+00.846	II	74.5692	0.8455	s-u-hmi	1.63(0.895)	3.251	4.57	√	√	
G080.315+01.332	II	80.3154	1.3317	s-pbsmi	1.83(0.59)	3.594	6.32	√		
G284.467-00.369	II	284.4673	-0.3693	s-u-hmi	1.75(0.42)	2.054	5.5	√		
G289.035-00.037	II	289.0348	-0.0368	spu-smi	1.24(0.58)	1.365	7.44	√		
G291.180-00.290	II	291.1799	-0.2899	sp–hmi	2.87(0.0)	2.127	7.34	√	√	
G295.106-01.678	II	295.1065	-1.6778	sp–hmi	2.16(0.11)	1.576	2.2	√	√	
G295.867-00.130	II	295.8669	-0.1301	spu-smi	2.46(1.47)	1.264	8.58	√		
G301.473-00.225	II	301.4734	-0.2254	spu-hmi	1.46(0.3)	3.909	6.39	√	√	
G303.566-00.854	II	303.5657	-0.8536	s-pbsmi	3.15(3.87)	1.135	11.27	√		
G303.846-00.363	II	303.8458	-0.3631	s-ubhmi	1.78(0.41)	2.325	11.49	√		√
G304.022+00.292	II	304.0224	0.2924	s-ubsmi	3.4(3.16)	4.44	4.67	√	√	
G305.254+00.081	II	305.2539	0.0806	s-pbhmi	1.48(0.0)	1.587	4.57	√		
G305.823-00.114	II	305.8225	-0.114	s-ubhmi	3.65(3.14)	2.273	5.92	√	√	√
G309.173-00.010	II	309.1727	-0.0099	s-pbsmi	1.44(0.26)	1.972	9.53	√	√	
G313.691+00.098	II	313.6911	0.098	s—smi	2.72(0.28)	2.097	8.52	√	√	
G313.758+00.254	II	313.7584	0.2539	s-ubhmi	2.42(1.83)	1.473	8.02	√		
G314.211+00.210	II	314.2112	0.21	s-u-smi	1.19(0.43)	1.335	7.45	√	√	
G317.873-01.054	II	317.8731	-1.0539	s-u-hmi	2.03(0.83)	2.097	3.47	√		
G321.148-00.529	II	321.1483	-0.5289	s-ubsmi	2.23(1.32)	1.482	3.84	√	√	√
G323.519-00.470	II	323.5186	-0.4699	s-u-hmi	1.34(0.0)	4.662	11.39	√		
G326.314-00.481	II	326.3136	-0.4807	sp–hmi	3.17(1.86)	1.963	10.3	√	√	
G326.920-00.021	II	326.9197	-0.0213	s-ubsmi	2.06(1.18)	1.03	3.32	√		
G327.894+00.149	II	327.8945	0.1485	s-ubhmi	3.79(1.86)	4.08	8.91	√		
G328.140-00.432	II	328.1401	-0.4317	s-ubhmi	1.71(0.27)	1.753	2.73	√	√	√
G328.335-00.528	II	328.3349	-0.5283	s-ubhmi	2.17(0.26)	1.09	2.54	√	√	
G329.014+00.985	II	329.0144	0.9849	s-u-hmi	0.93(0.0)	1.157	5.92	√	√	

Table 3 continued on next page

Table 3 *(continued)*

Name	Group	l	b	Model set	Stellar mass	Accretion rate	Distance	$\geqslant 870\ M_\odot R^{1.33}$	$\geqslant 1$ g/cm^2	Class II
					($M_\star$)	($\dot{M}_{\rm acc}$)				methanol maser
		°	°		$M_\odot$	$\times 10^{-4} M_\odot \mathrm{yr}^{-1}$	kpc			
(1)	(2)	(3)	(4)	(5)	(6)	(7)	(8)	(9)	(10)	(11)
G329.422-00.162	II	329.422	-0.1621	s-pbsmi	3.04(0.26)	1.794	4.35	√	√	
G329.705-00.343	II	329.7052	-0.3429	s-ubhmi	2.66(1.24)	1.959	11.44	√	√	
G331.083-00.475	II	331.0832	-0.4752	s-pbhmi	1.45(0.0)	1.106	3.91	√	√	
G331.434-00.283	II	331.4341	-0.2833	s-u-hmi	1.46(0.35)	4.843	4.87	√	√	
G332.350-00.436	II	332.3502	-0.4358	spu-hmi	1.22(0.61)	1.073	3.1	√	√	√
G332.725-00.621	II	332.7251	-0.6206	s-u-hmi	2.06(0.49)	4.186	3.8	√	√	√
G332.813-00.700	II	332.8129	-0.7004	s-ubsmi	2.69(2.31)	5.18	3.8	√	√	√
G333.203-00.046	II	333.2026	-0.0459	s-u-smi	1.18(0.39)	1.016	3.0	√	√	
G333.254-00.027	II	333.254	-0.0267	sp–hmi	2.71(0.49)	1.847	10.83	√		
G335.426-00.240	II	335.426	-0.2397	s-ubhmi	1.71(0.36)	5.653	2.95	√	√	√
G337.258-00.101	II	337.2578	-0.101	s-u-hmi	2.9(0.23)	3.679	11.17	√	√	√
G337.632-00.078	II	337.6318	-0.0785	s-pbhmi	2.48(2.13)	4.189	3.61	√	√	√
G337.697+00.381	II	337.6973	0.3814	s—smi	2.23(0.25)	2.056	10.76	√		
G338.325-00.409	II	338.3251	-0.409	s-u-hmi	1.92(1.1)	2.334	2.91	√	√	√
G338.467-00.010	II	338.4669	-0.0102	s-u-hmi	1.41(0.52)	2.085	5.94	√	√	
G340.768-01.013	II	340.7675	-1.0128	s-ubhmi	1.68(0.0)	1.623	2.0	√	√	
G340.822-01.028	II	340.8221	-1.0285	s-pbhmi	2.6(0.19)	1.136	2.0	√		
G342.061+00.421	II	342.0605	0.4205	spu-hmi	2.94(0.21)	3.068	4.51	√	√	
G342.821+00.383	II	342.8208	0.3825	s-u-hmi	1.28(0.23)	4.607	10.82	√	√	
G343.527-00.505	II	343.5272	-0.5053	s-pbhmi	1.72(1.02)	1.854	3.04	√	√	
G343.904-00.671	II	343.9037	-0.6709	s-ubhmi	2.35(1.1)	2.086	2.0	√	√	
G344.103-00.661	II	344.1031	-0.6613	s-u-smi	1.46(0.0)	1.548	2.0	√	√	
G346.355+00.105	II	346.3553	0.105	s-pbsmi	1.34(0.0)	1.73	5.91	√	√	
G348.003+00.192	II	348.0034	0.1916	sp–hmi	1.51(0.17)	1.836	5.89	√		
G350.749+00.505	II	350.7495	0.505	s-ubsmi	2.6(1.82)	3.002	4.29	√	√	
G354.688+00.508	II	354.6877	0.5083	s-pbhmi	1.26(0.0)	1.139	4.11	√	√	
G355.738+00.390	II	355.7384	0.39	s-ubsmi	2.37(1.35)	1.615	9.65	√		
G356.285+00.208	II	356.2851	0.2083	s-u-hmi	1.94(1.01)	2.805	9.59	√		
G356.344-00.070	II	356.3436	-0.0705	s-pbsmi	1.15(0.5)	1.609	6.81	√	√	
G357.523+00.195	II	357.5234	0.1946	sp–smi	2.71(1.56)	1.814	6.71	√	√	
G358.370-00.468	II	358.3703	-0.4675	s-u-smi	1.42(0.07)	1.343	1.63	√	√	√
G358.808-00.086	II	358.8083	-0.0856	s-pbhmi	1.94(1.31)	2.087	7.76	√	√	√
G011.904-00.141	III	11.9037	-0.1413	s-ubsmi	2.04(0.0)	3.105	3.67	√	√	√
G018.661+00.038	III	18.6608	0.0376	s-u-smi	3.52(2.66)	2.928	10.88	√	√	
G024.114-00.174	III	24.1138	-0.1745	sp–smi	4.75(7.18)	1.079	4.69	√	√	
G025.517-00.206	III	25.5171	-0.2061	s-u-hmi	3.8(3.7)	2.919	8.78	√		
G028.147-00.004	III	28.1467	-0.0044	s-ubsmi	3.63(3.86)	2.158	5.4	√	√	√
G030.446-00.359	III	30.4455	-0.3591	sp–smi	2.2(0.57)	4.669	8.54			
G031.496+00.177	III	31.4959	0.1771	spu-smi	2.46(2.42)	5.388	8.21	√	√	
G040.622-00.138	III	40.6221	-0.1381	s-u-hmi	3.75(4.72)	1.705	2.06	√	√	√
G053.331+00.040	III	53.3307	0.0399	s-pbhmi	2.76(2.42)	2.875	8.31			
G059.436+00.820	III	59.4364	0.8196	s-pbsmi	3.23(4.71)	3.753	6.28	√		√
G063.904-00.061	III	63.9038	-0.0605	s-ubsmi	2.95(2.48)	1.052	8.28	√		
G078.377+01.020	III	78.3769	1.0198	s-pbhmi	2.22(0.81)	2.615	3.56	√	√	
G087.556+00.502	III	87.5562	0.5016	s-pbsmi	1.65(0.83)	1.034	6.3	√		
G303.991+00.209	III	303.9912	0.2088	s-pbhmi	2.02(0.0)	1.021	4.66	√		
G304.367-00.336	III	304.3673	-0.3361	s-ubsmi	3.3(0.0)	4.594	11.95	√		√
G310.077-00.228	III	310.0767	-0.2277	spu-smi	1.8(0.5)	2.879	4.25	√		
G314.199+00.157	III	314.1992	0.1571	s-ubsmi	2.0(1.26)	3.222	7.57	√		
G322.385+00.533	III	322.3851	0.533	s-u-hmi	1.96(0.04)	1.555	3.36	√	√	
G322.521+00.637	III	322.5212	0.6366	s-pbhmi	2.02(0.0)	3.043	3.37	√	√	

Table 3 continued on next page

Table 3 *(continued)*

Name	Group	l	b	Model set	Stellar mass ($M_\star$)	Accretion rate ($\dot{M}_{\rm acc}$)	Distance	$\geqslant 870\ M_\odot R^{1.33}$	$\geqslant 1$ g/cm^2	Class II methanol maser
		°	°		$M_\odot$	$\times 10^{-4} M_\odot {\rm yr}^{-1}$	kpc			
(1)	(2)	(3)	(4)	(5)	(6)	(7)	(8)	(9)	(10)	(11)
G328.549+00.272	III	328.549	0.2716	spu-smi	3.93(6.16)	3.676	3.53	√	√	
G329.610+00.114	III	329.6098	0.1137	s-u-smi	6.13(10.03)	1.59	3.8	√	√	√
G337.110+00.348	III	337.1098	0.3483	spu-smi	2.83(2.5)	4.981	4.97	√		
G338.737+00.175	III	338.7372	0.1747	s-u-hmi	2.44(1.92)	1.078	3.29	√		
G340.746-01.002	III	340.7458	-1.0024	s-pbhmi	1.83(0.0)	1.963	2.0	√	√	
G340.937-00.231	III	340.9375	-0.2308	spu-hmi	1.21(0.02)	4.359	3.51	√	√	
G341.990-00.102	III	341.9905	-0.1019	s-pbhmi	1.84(0.58)	1.5	3.54	√		√
G343.721-00.223	III	343.7213	-0.2225	s-pbsmi	2.59(2.08)	1.139	2.0	√	√	
G352.158+00.402	III	352.1579	0.4025	sp–hmi	1.97(0.67)	3.006	2.0	√	√	
G356.596-00.503	III	356.5962	-0.5028	sp–smi	3.82(3.94)	4.177	12.86	√	√	
G357.533+00.236	III	357.5325	0.2363	s-pbhmi	2.12(0.86)	3.0	6.66	√	√	

NOTE—Catalog of WGOs as Candidate MYSOs.

We would like to thank the anonymous referees for valuable comments which improved the quality of the paper. We would to thank Dr. Zhiwei CHEN from Purple Mountain Observatory, Chinese Academy of Sciences for useful discussions on this paper. This work is supported by the Ministry of Science and Technology of China through grant 2010DFA02710, the Key Project of International Cooperation, and by the National Natural Science Foundation of China through grants 11503035, 11573036, 11373009, 11433008, 11403040 and 11403041. Guoyin ZHANG acknowledges support from China Postdoctoral Science Foundation (No.2021T140672), and National Natural Science foundation of China (No.U2031118).

REFERENCES

An, D., Ramírez, S. V., Sellgren, K., et al. 2011, ApJ, 736, 133, doi: 10.1088/0004-637X/736/2/133

Andre, P., Ward-Thompson, D., & Barsony, M. 1993, ApJ, 406, 122, doi: 10.1086/172425

Arce, H. G., Shepherd, D., Gueth, F., et al. 2007, in Protostars and Planets V, ed. B. Reipurth, D. Jewitt, & K. Keil, 245. https://arxiv.org/abs/astro-ph/0603071

Bachiller, R. 1996, ARA&A, 34, 111, doi: 10.1146/annurev.astro.34.1.111

Barnes, A. T., Longmore, S. N., Battersby, C., Bally, J., & Kruijssen, J. M. D. 2017, in The Multi-Messenger Astrophysics of the Galactic Centre, ed. R. M. Crocker, S. N. Longmore, & G. V. Bicknell, Vol. 322, 147–148, doi: 10.1017/S1743921316011856

Benjamin, R. A., Churchwell, E., Babler, B. L., et al. 2003, PASP, 115, 953, doi: 10.1086/376696

Bergin, E. A., & Tafalla, M. 2007, ARA&A, 45, 339, doi: 10.1146/annurev.astro.45.071206.100404

Beuther, H., Churchwell, E. B., McKee, C. F., & Tan, J. C. 2007, in Protostars and Planets V, ed. B. Reipurth, D. Jewitt, & K. Keil, 165. https://arxiv.org/abs/astro-ph/0602012

Bonnell, I., & Greaves, J. 2004, The formation of clusters: Comparing the star formation processes in the Rosette and Maddalena Clouds, Spitzer Proposal ID 3394

Bonnell, I. A., Bate, M. R., Clarke, C. J., & Pringle, J. E. 1997, MNRAS, 285, 201, doi: 10.1093/mnras/285.1.201

Breen, S. L., Ellingsen, S. P., Contreras, Y., et al. 2013, MNRAS, 435, 524, doi: 10.1093/mnras/stt1315

Bressert, E., Ginsburg, A., Bally, J., et al. 2012, ApJL, 758, L28, doi: 10.1088/2041-8205/758/2/L28

Busso, M., Gallino, R., & Wasserburg, G. J. 1999, ARA&A, 37, 239, doi: 10.1146/annurev.astro.37.1.239

Butler, M. J., & Tan, J. C. 2012, ApJ, 754, 5, doi: 10.1088/0004-637X/754/1/5

Caratti o Garatti, A., Stecklum, B., Garcia Lopez, R., et al. 2017, Nature Physics, 13, 276, doi: 10.1038/nphys3942

Chen, X., Ellingsen, S. P., Shen, Z.-Q., Titmarsh, A., & Gan, C.-G. 2011, ApJS, 196, 9, doi: 10.1088/0067-0049/196/1/9

Chen, X., Gan, C.-G., Ellingsen, S. P., et al. 2013, ApJS, 206, 9, doi: 10.1088/0067-0049/206/1/9

Chen, Z., Sun, W., Chini, R., et al. 2021, ApJ, 922, 90, doi: 10.3847/1538-4357/ac2151

Cho, S.-H., Yun, Y., Kim, J., et al. 2016, ApJ, 826, 157, doi: 10.3847/0004-637X/826/2/157

Churchwell, E., & GLIMPSE Team. 2001, in American Astronomical Society Meeting Abstracts, Vol. 198, American Astronomical Society Meeting Abstracts #198, 25.04

Churchwell, E., Babler, B. L., Meade, M. R., et al. 2009, PASP, 121, 213, doi: 10.1086/597811

Cragg, D. M., Johns, K. P., Godfrey, P. D., & Brown, R. D. 1992, MNRAS, 259, 203, doi: 10.1093/mnras/259.1.203

Crocker, R. M., Jones, D. I., Aharonian, F., et al. 2011, MNRAS, 413, 763, doi: 10.1111/j.1365-2966.2010.18170.x

Csengeri, T., Weiss, A., Wyrowski, F., et al. 2016, A&A, 585, A104, doi: 10.1051/0004-6361/201526639

Cyganowski, C. J., Brogan, C. L., Hunter, T. R., & Churchwell, E. 2009, ApJ, 702, 1615, doi: 10.1088/0004-637X/702/2/1615

Cyganowski, C. J., Brogan, C. L., Hunter, T. R., et al. 2017, MNRAS, 468, 3694, doi: 10.1093/mnras/stx043

Cyganowski, C. J., Koda, J., Rosolowsky, E., et al. 2013, ApJ, 764, 61, doi: 10.1088/0004-637X/764/1/61

Cyganowski, C. J., Whitney, B. A., Holden, E., et al. 2008, AJ, 136, 2391, doi: 10.1088/0004-6256/136/6/2391

Davis, C. J., Kumar, M. S. N., Sandell, G., et al. 2007, MNRAS, 374, 29, doi: 10.1111/j.1365-2966.2006.11163.x

Elia, D., Merello, M., Molinari, S., et al. 2021, MNRAS, 504, 2742, doi: 10.1093/mnras/stab1038

Ellingsen, S. P. 2006, ApJ, 638, 241, doi: 10.1086/498673

Fazio, G. G., Hora, J. L., Allen, L. E., et al. 2004, ApJS, 154, 10, doi: 10.1086/422843

Furuya, R. S., Kitamura, Y., Wootten, A., Claussen, M. J., & Kawabe, R. 2003, ApJS, 144, 71, doi: 10.1086/342749

Gallimore, J. F., Cool, R. J., Thornley, M. D., & McMullin, J. 2003, ApJ, 586, 306, doi: 10.1086/346266

Gallimore, J. F., Cool, R. J., Thornley, M. D., & McMullin, J. 2003, The Astrophysical Journal, 586, 306, doi: 10.1086/346266

Greene, T. P., Wilking, B. A., Andre, P., Young, E. T., & Lada, C. J. 1994, ApJ, 434, 614, doi: 10.1086/174763

Hasegawa, T., Morita, K., Okumura, S., et al. 1986, in Masers, Molecules, and Mass Outflows in Star Formation Regions, ed. A. D. Haschick, 275

Heiderman, A., Evans, Neal J., I., Allen, L. E., Huard, T., & Heyer, M. 2010, ApJ, 723, 1019, doi: 10.1088/0004-637X/723/2/1019

Herbig, G. H. 1962, Advances in Astronomy and Astrophysics, 1, 47, doi: 10.1016/B978-1-4831-9919-1.50006-6

Herwig, F. 2005, ARA&A, 43, 435, doi: 10.1146/annurev.astro.43.072103.150600

Higuchi, A. E., Hasegawa, T., Saigo, K., Sanhueza, P., & Chibueze, J. O. 2015, ApJ, 815, 106, doi: 10.1088/0004-637X/815/2/106

Hinz, J. L., Rieke, G. H., Yusef-Zadeh, F., et al. 2009, ApJS, 181, 227, doi: 10.1088/0067-0049/181/1/227

Hoare, M. G., Lumsden, S. L., Oudmaijer, R. D., et al. 2005, in Massive Star Birth: A Crossroads of Astrophysics, ed. R. Cesaroni, M. Felli, E. Churchwell, & M. Walmsley, Vol. 227, 370–375, doi: 10.1017/S174392130500476X

Hollenbach, D., Elitzur, M., & McKee, C. F. 2013, ApJ, 773, 70, doi: 10.1088/0004-637X/773/1/70

Hosokawa, T., Yorke, H. W., & Omukai, K. 2010, ApJ, 721, 478, doi: 10.1088/0004-637X/721/1/478

Hunter, T. R., Brogan, C. L., De Buizer, J. M., et al. 2021, ApJL, 912, L17, doi: 10.3847/2041-8213/abf6d9

Immer, K., Schuller, F., Omont, A., & Menten, K. M. 2012, A&A, 537, A121, doi: 10.1051/0004-6361/201117857

Jijina, J., & Adams, F. C. 1996, ApJ, 462, 874, doi: 10.1086/177201

Jones, B. M., Fuller, G. A., Breen, S. L., et al. 2020, MNRAS, 493, 2015, doi: 10.1093/mnras/staa233

Jones, O. C., Sharp, M. J., Reiter, M., et al. 2019, MNRAS, 490, 832, doi: 10.1093/mnras/stz2560

Kauffmann, J., & Pillai, T. 2010, ApJL, 723, L7, doi: 10.1088/2041-8205/723/1/L7

Kennicutt, R. C., & Evans, N. J. 2012, ARA&A, 50, 531, doi: 10.1146/annurev-astro-081811-125610

Kruijssen, J. M. D. 2012, MNRAS, 426, 3008, doi: 10.1111/j.1365-2966.2012.21923.x

Krumholz, M. R., & McKee, C. F. 2008, Nature, 451, 1082, doi: 10.1038/nature06620

Kuhn, M. A., de Souza, R. S., Krone-Martins, A., et al. 2021, ApJS, 254, 33, doi: 10.3847/1538-4365/abe465

Lada, C. J. 1987, in Star Forming Regions, ed. M. Peimbert & J. Jugaku, Vol. 115, 1

Lada, C. J., & Lada, E. A. 2003, ARA&A, 41, 57, doi: 10.1146/annurev.astro.41.011802.094844

Lada, C. J., Lombardi, M., & Alves, J. F. 2010, ApJ, 724, 687, doi: 10.1088/0004-637X/724/1/687

Ladeyschikov, D. A., Bayandina, O. S., & Sobolev, A. M. 2019, AJ, 158, 233, doi: 10.3847/1538-3881/ab4b4c

Larson, R. B. 1981, MNRAS, 194, 809, doi: 10.1093/mnras/194.4.809
López-Sepulcre, A., Cesaroni, R., & Walmsley, C. M. 2010, A&A, 517, A66, doi: 10.1051/0004-6361/201014252
Lumsden, S. L., Hoare, M. G., Urquhart, J. S., et al. 2013, ApJS, 208, 11, doi: 10.1088/0067-0049/208/1/11
Mac Low, M.-M., Elitzur, M., Stone, J. M., & Konigl, A. 1994, ApJ, 427, 914, doi: 10.1086/174196
Marton, G., Tóth, L. V., Paladini, R., et al. 2016, MNRAS, 458, 3479, doi: 10.1093/mnras/stw398
Matsuura, M., Yamamura, I., Murakami, H., et al. 2000, PASJ, 52, 895, doi: 10.1093/pasj/52.5.895
McKee, C. F., & Tan, J. C. 2002, Nature, 416, 59, doi: 10.1038/416059a
—. 2003, ApJ, 585, 850, doi: 10.1086/346149
Mège, P., Russeil, D., Zavagno, A., et al. 2021, A&A, 646, A74, doi: 10.1051/0004-6361/202038956
Molinari, S., Brand, J., Cesaroni, R., & Palla, F. 1996, A&A, 308, 573
Molinari, S., Swinyard, B., Bally, J., et al. 2010, PASP, 122, 314, doi: 10.1086/651314
Moser, E., Liu, M., Tan, J. C., et al. 2020, ApJ, 897, 136, doi: 10.3847/1538-4357/ab96c1
Motte, F., Bontemps, S., & Louvet, F. 2018, ARA&A, 56, 41, doi: 10.1146/annurev-astro-091916-055235
Nakashima, J.-i., & Deguchi, S. 2000, PASJ, 52, L43, doi: 10.1093/pasj/52.5.L43
Noriega-Crespo, A., Morris, P., Marleau, F. R., et al. 2004, ApJS, 154, 352, doi: 10.1086/422819
Olivier, G. M., Lopez, L. A., Rosen, A. L., et al. 2021, ApJ, 908, 68, doi: 10.3847/1538-4357/abd24a
Pilbratt, G. L., Riedinger, J. R., Passvogel, T., et al. 2010, A&A, 518, L1, doi: 10.1051/0004-6361/201014759
Reach, W. T., Rho, J., Tappe, A., et al. 2006, AJ, 131, 1479, doi: 10.1086/499306
Reid, M. J. 2002, in Cosmic Masers: From Proto-Stars to Black Holes, ed. V. Migenes & M. J. Reid, Vol. 206, 506
Robitaille, T. P. 2017, A&A, 600, A11, doi: 10.1051/0004-6361/201425486
Robitaille, T. P., Whitney, B. A., Indebetouw, R., Wood, K., & Denzmore, P. 2006, ApJS, 167, 256, doi: 10.1086/508424
Sanhueza, P., Jackson, J. M., Foster, J. B., et al. 2012, ApJ, 756, 60, doi: 10.1088/0004-637X/756/1/60
Schmidt, M. 1959, ApJ, 129, 243, doi: 10.1086/146614
Schuller, F., Menten, K. M., Contreras, Y., et al. 2009, A&A, 504, 415, doi: 10.1051/0004-6361/200811568
Shu, F. H., Adams, F. C., & Lizano, S. 1987, ARA&A, 25, 23, doi: 10.1146/annurev.aa.25.090187.000323
Smith, M. D., & Rosen, A. 2005, MNRAS, 357, 1370, doi: 10.1111/j.1365-2966.2005.08785.x
Smith, R. J., Longmore, S., & Bonnell, I. 2009, MNRAS, 400, 1775, doi: 10.1111/j.1365-2966.2009.15621.x
Snyder, L. E., & Buhl, D. 1974, ApJL, 189, L31, doi: 10.1086/181457
Sobolev, A. M., Cragg, D. M., Ellingsen, S. P., et al. 2007, Proceedings of the International Astronomical Union, 3, 81–88, doi: 10.1017/S1743921307012616
Stecklum, B., Heese, S., Wolf, S., et al. 2017, arXiv e-prints, arXiv:1712.01451. https://arxiv.org/abs/1712.01451
Stecklum, B., Wolf, V., Linz, H., et al. 2021, A&A, 646, A161, doi: 10.1051/0004-6361/202039645
Szymczak, M., Pillai, T., & Menten, K. M. 2005, A&A, 434, 613, doi: 10.1051/0004-6361:20042437
Tout, C. A., Pols, O. R., Eggleton, P. P., & Han, Z. 1996, MNRAS, 281, 257, doi: 10.1093/mnras/281.1.257
Towner, A. P. M., Brogan, C. L., Hunter, T. R., Cyganowski, C. J., & Friesen, R. K. 2019, ApJ, 875, 135, doi: 10.3847/1538-4357/ab1140
Towner, A. P. M., Brogan, C. L., Hunter, T. R., et al. 2017, ApJS, 230, 22, doi: 10.3847/1538-4365/aa73d8
Urquhart, J. S., Moore, T. J. T., Csengeri, T., et al. 2014, MNRAS, 443, 1555, doi: 10.1093/mnras/stu1207
Urquhart, J. S., Wells, M. R. A., Pillai, T., et al. 2022, MNRAS, 510, 3389, doi: 10.1093/mnras/stab3511
Velusamy, T., Langer, W. D., & Marsh, K. A. 2007, ApJL, 668, L159, doi: 10.1086/522929
Wang, Y., Beuther, H., Bik, A., et al. 2011, A&A, 527, A32, doi: 10.1051/0004-6361/201015543
Wenger, M., Ochsenbein, F., Egret, D., et al. 2000, A&AS, 143, 9, doi: 10.1051/aas:2000332
Wright, E. L., Eisenhardt, P. R. M., Mainzer, A. K., et al. 2010, AJ, 140, 1868, doi: 10.1088/0004-6256/140/6/1868
—. 2019, AllWISE Source Catalog, IPAC, doi: 10.26131/IRSA1
Yorke, H. W., & Sonnhalter, C. 2002, ApJ, 569, 846, doi: 10.1086/339264
Yusef-Zadeh, F., Hewitt, J. W., Arendt, R. G., et al. 2009, ApJ, 702, 178, doi: 10.1088/0004-637X/702/1/178
Zapata, L. A., Menten, K., Reid, M., & Beuther, H. 2009, ApJ, 691, 332, doi: 10.1088/0004-637X/691/1/332
Zhang, C., Zhang, G.-Y., Li, J.-Z., & Li, X.-M. 2022, Research in Astronomy and Astrophysics, 22, 055012, doi: 10.1088/1674-4527/ac5bc7
Zhang, G.-Y., Xu, J.-L., Vasyunin, A. I., et al. 2018, A&A, 620, A163, doi: 10.1051/0004-6361/201833622
Zhang, Y., & Tan, J. C. 2011, ApJ, 733, 55, doi: 10.1088/0004-637X/733/1/55

Zinnecker, H., & Yorke, H. W. 2007, ARA&A, 45, 481,
doi: 10.1146/annurev.astro.44.051905.092549